A&A 594, A20 (2016)
DOI: 10.1051/0004-6361/201525898

Astronomy & Astrophysics
Special feature

Planck 2015 results

Planck 2015 results
XX. Constraints on inflation

Planck Collaboration: P. A. R. Ade[99], N. Aghanim[66], M. Arnaud[82], F. Arroja[74,88], M. Ashdown[78,6], J. Aumont[66], C. Baccigalupi[97], M. Ballardini[54,56,37], A. J. Banday[112,11], R. B. Barreiro[73], N. Bartolo[36,74], E. Battaner[114,115], K. Benabed[67,111], A. Benoît[64], A. Benoit-Lévy[28,67,111], J.-P. Bernard[112,11], M. Bersanelli[40,55], P. Bielewicz[92,11,97], J. J. Bock[75,13], A. Bonaldi[76], L. Bonavera[73], J. R. Bond[10], J. Borrill[16,104], F. R. Bouchet[67,102], F. Boulanger[66], M. Bucher[1,⋆], C. Burigana[54,38,56], R. C. Butler[54], E. Calabrese[107], J.-F. Cardoso[83,1,67], A. Catalano[84,81], A. Challinor[70,78,14], A. Chamballu[82,18,66], R.-R. Chary[63], H. C. Chiang[32,7], P. R. Christensen[93,43], S. Church[106], D. L. Clements[62], S. Colombi[67,111], L. P. L. Colombo[27,75], C. Combet[84], D. Contreras[26], F. Couchot[80], A. Coulais[81], B. P. Crill[75,13], A. Curto[73,6,78], F. Cuttaia[54], L. Danese[97], R. D. Davies[76], R. J. Davis[76], P. de Bernardis[39], A. de Rosa[54], G. de Zotti[51,97], J. Delabrouille[1], F.-X. Désert[60], J. M. Diego[73], H. Dole[66,65], S. Donzelli[55], O. Doré[75,13], M. Douspis[66], A. Ducout[67,62], X. Dupac[46], G. Efstathiou[70], F. Elsner[28,67,111], T. A. Enßlin[89], H. K. Eriksen[71], J. Fergusson[14], F. Finelli[54,56,⋆], O. Forni[112,11], M. Frailis[53], A. A. Fraisse[32], E. Franceschi[54], A. Frejsel[93], A. Frolov[101], S. Galeotta[53], S. Galli[77], K. Ganga[1], C. Gauthier[1,88], M. Giard[112,11], Y. Giraud-Héraud[1], E. Gjerløw[71], J. González-Nuevo[23,73], K. M. Górski[75,116], S. Gratton[78,70], A. Gregorio[41,53,59], A. Gruppuso[54], J. E. Gudmundsson[109,95,32], J. Hamann[110,108], W. Handley[78,6], F. K. Hansen[71], D. Hanson[90,75,10], D. L. Harrison[70,78], S. Henrot-Versillé[80], C. Hernández-Monteagudo[15,89], D. Herranz[73], S. R. Hildebrandt[75,13], E. Hivon[67,111], M. Hobson[6], W. A. Holmes[75], A. Hornstrup[19], W. Hovest[89], Z. Huang[10], K. M. Huffenberger[30], G. Hurier[66], A. H. Jaffe[62], T. R. Jaffe[112,11], W. C. Jones[32], M. Juvela[31], E. Keihänen[31], R. Keskitalo[16], J. Kim[89], T. S. Kisner[86], R. Kneissl[45,8], J. Knoche[89], M. Kunz[20,66,3], H. Kurki-Suonio[31,50], G. Lagache[5,66], A. Lähteenmäki[2,50], J.-M. Lamarre[81], A. Lasenby[6,78], M. Lattanzi[38], C. R. Lawrence[75], R. Leonardi[9], J. Lesgourgues[68,110], F. Levrier[81], A. Lewis[29], M. Liguori[36,74], P. B. Lilje[71], M. Linden-Vørnle[19], M. López-Caniego[46,73], P. M. Lubin[34], Y.-Z. Ma[26,76], J. F. Macías-Pérez[84], G. Maggio[53], D. Maino[40,55], N. Mandolesi[54,38], A. Mangilli[66,80], M. Maris[53], P. G. Martin[10], E. Martínez-González[73], S. Masi[39], S. Matarrese[36,74,48], P. McGehee[63], P. R. Meinhold[34], A. Melchiorri[39,57], L. Mendes[46], A. Mennella[40,55], M. Migliaccio[70,78], S. Mitra[61,75], M.-A. Miville-Deschênes[66,10], D. Molinari[73,54], A. Moneti[67], L. Montier[112,11], G. Morgante[54], D. Mortlock[62], A. Moss[100], M. Münchmeyer[67], D. Munshi[99], J. A. Murphy[91], P. Naselsky[94,44], F. Nati[32], P. Natoli[38,4,54], C. B. Netterfield[24], H. U. Nørgaard-Nielsen[19], F. Noviello[76], D. Novikov[87], I. Novikov[93,87], C. A. Oxborrow[19], F. Paci[97], L. Pagano[39,57], F. Pajot[66], R. Paladini[63], S. Pandolfi[21], D. Paoletti[54,56], F. Pasian[53], G. Patanchon[1], T. J. Pearson[13,63], H. V. Peiris[28], O. Perdereau[80], L. Perotto[84], F. Perrotta[97], V. Pettorino[49], F. Piacentini[39], M. Piat[1], E. Pierpaoli[27], D. Pietrobon[75], S. Plaszczynski[80], E. Pointecouteau[112,11], G. Polenta[4,52], L. Popa[69], G. W. Pratt[82], G. Prézeau[13,75], S. Prunet[67,111], J.-L. Puget[66], J. P. Rachen[25,89], W. T. Reach[113], R. Rebolo[72,17,22], M. Reinecke[89], M. Remazeilles[76,66,1], C. Renault[84], A. Renzi[42,58], I. Ristorcelli[112,11], G. Rocha[75,13], C. Rosset[1], M. Rossetti[40,55], G. Roudier[1,81,75], M. Rowan-Robinson[62], J. A. Rubiño-Martín[72,22], B. Rusholme[63], M. Sandri[54], D. Santos[84], M. Savelainen[31,50], G. Savini[96], D. Scott[26], M. D. Seiffert[75,13], E. P. S. Shellard[14], M. Shiraishi[36,74], L. D. Spencer[99], V. Stolyarov[6,105,79], R. Stompor[1], R. Sudiwala[99], R. Sunyaev[89,103], D. Sutton[70,78], A.-S. Suur-Uski[31,50], J.-F. Sygnet[67], J. A. Tauber[47], L. Terenzi[98,54], L. Toffolatti[23,73,54], M. Tomasi[40,55], M. Tristram[80], T. Trombetti[54], M. Tucci[20], J. Tuovinen[12], L. Valenziano[54], J. Valiviita[31,50], B. Van Tent[85], P. Vielva[73], F. Villa[54], L. A. Wade[75], B. D. Wandelt[67,111,35], I. K. Wehus[75,71], M. White[33], D. Yvon[18], A. Zacchei[53], J. P. Zibin[26], and A. Zonca[34]

(Affiliations can be found after the references)

Received 14 February 2015 / Accepted 3 March 2016

ABSTRACT

We present the implications for cosmic inflation of the *Planck* measurements of the cosmic microwave background (CMB) anisotropies in both temperature and polarization based on the full *Planck* survey, which includes more than twice the integration time of the nominal survey used for the 2013 release papers. The *Planck* full mission temperature data and a first release of polarization data on large angular scales measure the spectral index of curvature perturbations to be $n_s = 0.968 \pm 0.006$ and tightly constrain its scale dependence to $\mathrm{d}n_s/\mathrm{d}\ln k = -0.003 \pm 0.007$ when combined with the *Planck* lensing likelihood. When the *Planck* high-ℓ polarization data are included, the results are consistent and uncertainties are further reduced. The upper bound on the tensor-to-scalar ratio is $r_{0.002} < 0.11$ (95% CL). This upper limit is consistent with the B-mode polarization constraint $r < 0.12$ (95% CL) obtained from a joint analysis of the BICEP2/Keck Array and *Planck* data. These results imply that $V(\phi) \propto \phi^2$ and natural inflation are now disfavoured compared to models predicting a smaller tensor-to-scalar ratio, such as R^2 inflation. We search for several physically motivated deviations from a simple power-law spectrum of curvature perturbations, including those motivated by a reconstruction of the inflaton potential not relying on the slow-roll approximation. We find that such models are not preferred, either according to a Bayesian model comparison or according to a frequentist simulation-based analysis. Three independent methods reconstructing the primordial power spectrum consistently recover a featureless and smooth $\mathcal{P}_{\mathcal{R}}(k)$ over the range of scales $0.008\,\mathrm{Mpc}^{-1} \lesssim k \lesssim 0.1\,\mathrm{Mpc}^{-1}$. At large scales, each method finds deviations from a power law, connected to a deficit at multipoles $\ell \approx 20$–40 in the temperature power spectrum, but at an uncompelling statistical significance owing to the large cosmic variance present at these multipoles. By combining power spectrum and non-Gaussianity bounds, we constrain models with generalized Lagrangians, including Galileon models and axion monodromy models. The *Planck* data are consistent with adiabatic primordial perturbations, and the estimated values for the parameters of the base Λ cold dark matter (ΛCDM) model are not significantly altered when more general initial conditions are admitted. In correlated mixed adiabatic and isocurvature models, the 95% CL upper bound for the non-adiabatic contribution to the observed CMB temperature variance is $|\alpha_{\mathrm{non\text{-}adi}}| < 1.9\%$, 4.0%, and 2.9% for CDM, neutrino density, and neutrino velocity isocurvature modes, respectively. We have tested inflationary models producing an anisotropic modulation of the primordial curvature power spectrum finding that the dipolar modulation in the CMB temperature field induced by a CDM isocurvature perturbation is not preferred at a statistically significant level. We also establish tight constraints on a possible quadrupolar modulation of the curvature perturbation. These results are consistent with the *Planck* 2013 analysis based on the nominal mission data and further constrain slow-roll single-field inflationary models, as expected from the increased precision of *Planck* data using the full set of observations.

Key words. cosmic background radiation – cosmology: theory – early Universe – inflation

⋆ Corresponding author: Martin Bucher, e-mail: bucher@apc.univ-paris7.fr; Fabio Finelli, e-mail: finelli@iasfbo.inaf.it

1. Introduction

The precise measurements by *Planck*[1] of the cosmic microwave background (CMB) anisotropies covering the entire sky and over a broad range of scales, from the largest visible down to a resolution of approximately 5′, provide a powerful probe of cosmic inflation, as detailed in the *Planck* 2013 inflation paper (Planck Collaboration XXII 2014, hereafter PCI13). In the 2013 results, the robust detection of the departure of the scalar spectral index from exact scale invariance, i.e., $n_s < 1$, at more than 5σ confidence, as well as the lack of the observation of any statistically significant running of the spectral index, were found to be consistent with simple slow-roll models of inflation. Single-field inflationary models with a standard kinetic term were also found to be compatible with the new tight upper bounds on the primordial non-Gaussianity parameters f_{NL} reported in Planck Collaboration XXVI (2014). No evidence of isocurvature perturbations as generated in multi-field inflationary models (PCI13) or by cosmic strings or topological defects was found (Planck Collaboration XXV 2014). The *Planck* 2013 results overall favoured the simplest inflationary models. However, we noted an amplitude deficit for multipoles $\ell \lesssim 40$ whose statistical significance relative to the six-parameter base Λ cold dark matter (ΛCDM) model is only about 2σ, as well as other anomalies on large angular scales but also without compelling statistical significance (Planck Collaboration XXIII 2014). The constraint on the tensor-to-scalar ratio, $r < 0.12$ at 95% CL, inferred from the temperature power spectrum alone, combined with the determination of n_s, suggested models with concave potentials.

This paper updates the implications for inflation in the light of the *Planck* full mission temperature and polarization data. The *Planck* 2013 cosmology results included only the nominal mission, comprising the first 14 months of the data taken, and used only the temperature data. However, the full mission includes the full 29 months of scientific data taken by the cryogenically cooled high frequency instrument (HFI; which ended when the ^{3}He/^{4}He supply for the final stage of the cooling chain ran out) and the approximately four years of data taken by the low frequency instrument (LFI), which covered a longer period than the HFI because the LFI did not rely on cooling down to 100 mK for its operation. For a detailed discussion of the new likelihood and a comparison with the 2013 likelihood, we refer the reader to Planck Collaboration XI (2016) and Planck Collaboration XIII (2016), but we mention here some highlights of the differences between the 2013 and 2015 data processing and likelihoods: (1) improvements in the data processing such as beam characterization and absolute calibration at each frequency result in a better removal of systematic effects and (2) the 2015 temperature high-ℓ likelihood uses half-mission cross-power spectra over more of the sky, owing to less aggressive Galactic cuts. The use of polarization information in the 2015 likelihood release contributes to the constraining power of *Planck* in two principal ways: (1) the measurement of the E-mode polarization at large angular scales (presently based on the 70 GHz channel) constrains the reionization optical depth, τ, independently of other estimates using ancillary data; and (2) the measurement of the *TE* and *EE* spectra at $\ell \geq 30$ at the same frequencies used for the *TT* spectra (100, 143, and 217 GHz) helps break parameter degeneracies, particularly for extended cosmological models (beyond the baseline six-parameter model). A full analysis of the *Planck* low-ℓ polarization is still in progress and will be the subject of another forthcoming set of *Planck* publications.

The *Planck* 2013 results have sparked a revival of interest in several aspects of inflationary models. We mention here a few examples without the ambition to be exhaustive. A lively debate arose on the conceptual problems of some of the inflationary models favoured by the *Planck* 2013 data (Ijjas et al. 2013, 2014; Guth et al. 2014; Linde 2014). The interest in the R^2 inflationary model originally proposed by Starobinsky (1980) increased, since its predictions for cosmological fluctuations (Mukhanov & Chibisov 1981; Starobinsky 1983) are compatible with the *Planck* 2013 results (PCI13). It has been shown that supergravity motivates a potential similar to the Einstein gravity conformal representation of the R^2 inflationary model in different contexts (Ellis et al. 2013a,b; Buchmüller et al. 2013; Farakos et al. 2013; Ferrara et al. 2013b). A similar potential can also be generated by spontaneous breaking of conformal symmetry (Kallosh & Linde 2013b).

The constraining power of *Planck* also motivated a comparison between large numbers of inflationary models (Martin et al. 2014) and stimulated different perspectives on how best to compare theoretical inflationary predictions with observations based on the parameterized dependence of the Hubble parameter on the scale factor during inflation (Mukhanov 2013; Binétruy et al. 2015; Garcia-Bellido & Roest 2014). The interpretation of the asymmetries on large angular scales (Planck Collaboration XXIII 2014) also prompted a reanalysis of the primordial dipole modulation (Lyth 2013; Liddle & Cortês 2013; Kanno et al. 2013) of curvature perturbations during inflation.

Another recent development has been the renewed interest in possible tensor modes generated during inflation, sparked by the BICEP2 results (BICEP2 Collaboration 2014a,b). The BICEP2 team suggested that the *B*-mode polarization signal detected at $50 < \ell < 150$ at a single frequency (150 GHz) might be of primordial origin. However, a crucial step in this possible interpretation was excluding an explanation based on polarized thermal dust emission from our Galaxy. The BICEP2 team put forward a number of models to estimate the likely contribution from dust, but at the time relevant observational data were lacking, and this modelling involved a high degree of extrapolation. If dust polarization were negligible in the observed patch of 380 deg^2, this interpretation would lead to a tensor-to-scalar ratio of $r = 0.2^{+0.07}_{-0.05}$ for a scale-invariant spectrum. A value of $r \approx 0.2$, as suggested by BICEP2 Collaboration (2014b), would have obviously changed the *Planck* 2013 perspective according to which slow-roll inflationary models are favoured, and such a high value of r would also have required a strong running of the scalar spectral index, or some other modification from a simple power-law spectrum, to reconcile the contribution of gravitational waves to temperature anisotropies at low multipoles with the observed *TT* spectrum.

The interpretation of the *B*-mode signal in terms of gravitational waves *alone* presented in BICEP2 Collaboration (2014b) was later cast in doubt by *Planck* measurements of dust polarization at 353 GHz (Planck Collaboration Int. XIX 2015; Planck Collaboration Int. XX 2015; Planck Collaboration Int. XXI 2015; Planck Collaboration Int. XXII 2015). The *Planck* measurements characterized the frequency dependence of intensity and polarization of the Galactic dust emission, and moreover showed that the polarization fraction is higher than expected

[1] *Planck* (http://www.esa.int/Planck) is a project of the European Space Agency (ESA) with instruments provided by two scientific consortia funded by ESA member states and led by Principal Investigators from France and Italy, telescope reflectors provided through a collaboration between ESA and a scientific consortium led and funded by Denmark, and additional contributions from NASA (USA).

in regions of low dust emission. With the help of the *Planck* measurements of Galactic dust properties (Planck Collaboration Int. XIX 2015), it was shown that the interpretation of the *B*-mode polarization signal in terms of a primordial tensor signal plus a lensing contribution was not statistically preferred to an explanation based on the expected dust signal at 150 GHz plus a lensing contribution (see also Flauger et al. 2014a; Mortonson & Seljak 2014). Subsequently, Planck Collaboration Int. XXX (2016) extrapolated the *Planck* *B*-mode power spectrum of dust polarization at 353 GHz over the multipole range $40 < \ell < 120$ to 150 GHz, showing that the *B*-mode polarization signal detected by BICEP2 could be entirely due to dust.

More recently, a BICEP2/Keck Array-*Planck* (BKP) joint analysis (BICEP2/Keck Array and Planck Collaborations 2015, herafter BKP) combined the high-sensitivity *B*-mode maps from BICEP2 and Keck Array with the *Planck* maps at higher frequencies where dust emission dominates. A study of the cross-correlations of all these maps in the BICEP2 field found the absence of any statistically significant evidence for primordial gravitational waves, setting an upper limit of $r < 0.12$ at 95% CL (BKP). Although this upper limit is numerically almost identical to the *Planck* 2013 result obtained combining the nominal mission temperature data with WMAP polarization to remove parameter degeneracies (Planck Collaboration XVI 2014; Planck Collaboration XXII 2014), the BKP upper bound is much more robust against modifications of the inflationary model, since *B* modes are insensitive to the shape of the predicted scalar anisotropy pattern. In Sect. 13 we explore how the recent BKP analysis constrains inflationary models.

This paper is organized as follows. Section 2 briefly reviews the additional information on the primordial cosmological fluctuations encoded in the polarization angular power spectrum. Section 3 describes the statistical methodology as well as the *Planck* and other likelihoods used throughout the paper. Sections 4 and 5 discuss the *Planck* 2015 constraints on scalar and tensor fluctuations, respectively. Section 6 is dedicated to constraints on the slow-roll parameters and provides a Bayesian comparison of selected slow-roll inflationary models. In Sect. 7 we reconstruct the inflaton potential and the Hubble parameter as a Taylor expansion of the inflaton in the observable range without relying on the slow-roll approximation. The reconstruction of the curvature perturbation power spectrum is presented in Sect. 8. The search for parameterized features is presented in Sect. 9, and combined constraints from the *Planck* 2015 power spectrum and primordial non-Gaussianity derived in Planck Collaboration XVII (2016) are presented in Sect. 10. The analysis of isocurvature perturbations combined and correlated with curvature perturbations is presented in Sect. 11. In Sect. 12 we study the implications of relaxing the assumption of statistical isotropy of the primordial fluctuations. We discuss two examples of *anisotropic* inflation in light of the tests of isotropy performed in Planck Collaboration XVI (2016). Section 14 presents some concluding remarks.

2. What new information does polarization provide?

This section provides a short theoretical overview of the extra information provided by polarization data over that of temperature alone. (More details can be found in White et al. 1994; Ma & Bertschinger 1995; Bucher 2015, and references therein.) In Sect. 2 of the *Planck* 2013 inflation paper (PCI13), we gave an overview of the relation between the inflationary potential and the three-dimensional primordial scalar and tensor power spectra, denoted as $\mathcal{P}_{\mathcal{R}}(k)$ and $\mathcal{P}_{\rm t}(k)$, respectively. (The scalar variable $\mathcal{R}$ is defined precisely in Sect. 3.) We shall not repeat the discussion there, instead referring the reader to PCI13 and references therein.

Under the assumption of statistical isotropy, which is predicted in all simple models of inflation, the two-point correlations of the CMB anisotropies are described by the angular power spectra $C_\ell^{\rm TT}$, $C_\ell^{\rm TE}$, $C_\ell^{\rm EE}$, and C_ℓ^{BB}, where ℓ is the multipole number. (See Kamionkowski et al. 1997; Zaldarriaga & Seljak 1997; Seljak & Zaldarriaga 1997; Hu & White 1997; Hu et al. 1998 and references therein for early discussions elucidating the role of polarization.) In principle, one could also envisage measuring C_ℓ^{BT} and C_ℓ^{BE}, but in theories where parity symmetry is not explicitly or spontaneously broken, the expectation values for these cross spectra (i.e., the theoretical cross spectra) vanish, although the observed realizations of the cross spectra are not exactly zero because of cosmic variance.

The CMB angular power spectra are related to the three-dimensional scalar and tensor power spectra via the transfer functions $\Delta^{\rm s}_{\ell,\mathcal{A}}(k)$ and $\Delta^{\rm t}_{\ell,\mathcal{A}}(k)$, so that the contributions from scalar and tensor perturbations are

$$C_\ell^{\mathcal{AB},{\rm s}} = \int_0^\infty \frac{{\rm d}k}{k}\, \Delta^{\rm s}_{\ell,\mathcal{A}}(k)\, \Delta^{\rm s}_{\ell,\mathcal{B}}(k)\, \mathcal{P}_{\mathcal{R}}(k) \tag{1}$$

and

$$C_\ell^{\mathcal{AB},{\rm t}} = \int_0^\infty \frac{{\rm d}k}{k}\, \Delta^{\rm t}_{\ell,\mathcal{A}}(k)\, \Delta^{\rm t}_{\ell,\mathcal{B}}(k)\, \mathcal{P}_{\rm t}(k), \tag{2}$$

respectively, where $\mathcal{A}, \mathcal{B} = T, E, B$. The scalar and tensor primordial perturbations are uncorrelated in the simplest models, so the scalar and tensor power spectra add in quadrature, meaning that

$$C_\ell^{\mathcal{AB},{\rm tot}} = C_\ell^{\mathcal{AB},{\rm s}} + C_\ell^{\mathcal{AB},{\rm t}}. \tag{3}$$

Roughly speaking, the form of the linear transformations encapsulated in the transfer functions $\Delta^{\rm s}_{\ell,\mathcal{A}}(k)$ and $\Delta^{\rm t}_{\ell,\mathcal{A}}(k)$ probe the late time physics, whereas the primordial power spectra $\mathcal{P}_{\mathcal{R}}(k)$ and $\mathcal{P}_{\rm t}(k)$ are solely determined by the primordial Universe, perhaps not so far below the Planck scale if large-field inflation turns out to be correct.

To better understand this connection, it is useful to plot and compare the shapes of the transfer functions for representative values of ℓ and characterize their qualitative behavior. Referring to Fig. 1, we emphasize the following qualitative features:

1. For the scalar mode transfer functions, of which only $\Delta^{\rm s}_{\ell,T}(k)$ and $\Delta^{\rm s}_{\ell,E}(k)$ are non-vanishing (because to linear order, a three-dimensional scalar mode cannot contribute to the *B* mode of the polarization), both transfer functions start to rise at more or less the same small values of k (due to the centrifugal barrier in the Bessel differential equation), but $\Delta^{\rm s}_{\ell,E}(k)$ falls off much faster at large k and thus smooths sharp features in $\mathcal{P}_{\mathcal{R}}(k)$ to a lesser extent than $\Delta^{\rm s}_{\ell,T}(k)$. This means that polarization is more powerful than temperature for reconstructing possible sharp features in the scalar primordial power spectrum provided that the required signal-to-noise is available.
2. For the tensor modes, $\Delta^{\rm t}_{\ell,T}(k)$ starts rising at about the same small k as $\Delta^{\rm s}_{\ell,T}(k)$ and $\Delta^{\rm s}_{\ell,E}(k)$ but falls off faster with increasing k than $\Delta^{\rm s}_{\ell,T}(k)$. On the other hand, the polarization components, $\Delta^{\rm t}_{\ell,E}(k)$ and $\Delta^{\rm t}_{\ell,B}(k)$, have a shape completely different from any of the other transfer functions. The shape of

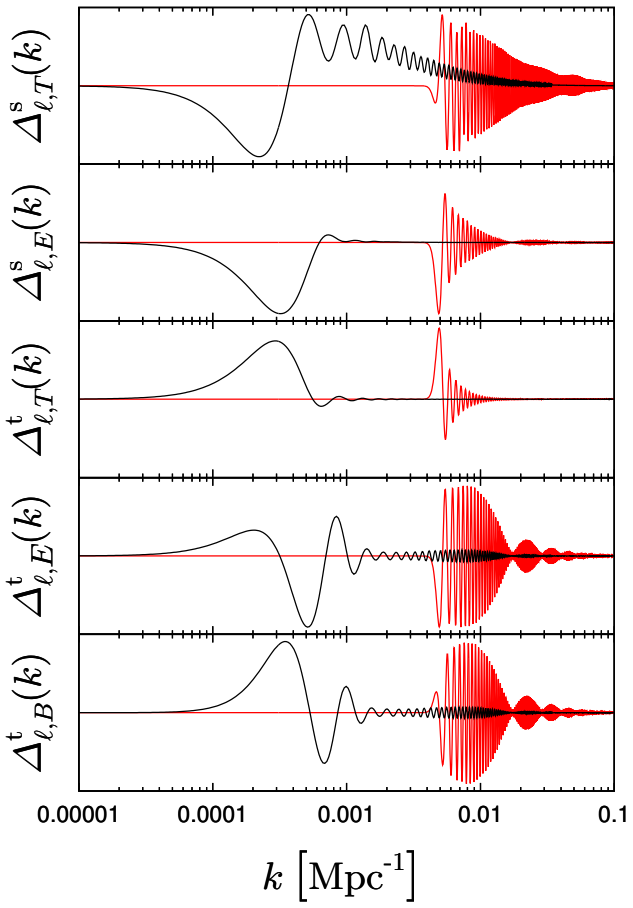

Fig. 1. Comparison of transfer functions for the scalar and tensor modes. The CMB transfer functions $\Delta^{\rm s}_{\ell,\mathcal{A}}(k)$ and $\Delta^{\rm t}_{\ell,\mathcal{A}}(k)$, where $\mathcal{A} = T, E, B$, define the linear transformations mapping the primordial scalar and tensor cosmological perturbations to the CMB anisotropies as seen by us on the sky today. These functions are plotted for two representative values of the multipole number: $\ell = 2$ (in black) and $\ell = 65$ (in red).

$\Delta^{\rm t}_{\ell,E}(k)$ and $\Delta^{\rm t}_{\ell,B}(k)$ is much wider in $\ln(k)$ than the scalar polarization transfer function, with a variance ranging from 0.5 to 1.0 decades. These functions exhibit several oscillations with a period smaller than that for scalar transfer functions, due to the difference between the sound velocity for scalar fluctuations and the light velocity for gravitational waves (Polarski & Starobinsky 1996; Lesgourgues et al. 2000).

Regarding the scalar primordial cosmological perturbations, the power spectrum of the E-mode polarization provides an important consistency check. As we explore in Sects. 8 and 9, to some extent the fit of the temperature power spectrum can be improved by allowing a complicated form for the primordial power spectrum (relative to a simple power law), but the $C_\ell^{\rm TE}$ and $C_\ell^{\rm EE}$ power spectra provide independent information. Moreover, in multi-field inflationary models, in which isocurvature modes may have been excited (possibly correlated amongst themselves as well as with the adiabatic mode), polarization information provides a powerful way to break degeneracies (see, e.g., Bucher et al. 2001).

The inability of scalar modes to generate B-mode polarization (apart from the effects of lensing) has an important consequence. For the primordial tensor modes, polarization information, especially information concerning the B-mode polarization, offers powerful potential for discovery or for establishing upper bounds. *Planck* 2013 and WMAP established upper bounds on a possible tensor mode contribution using $C_\ell^{\rm TT}$ alone, but these bounds crucially relied on assuming a simple form for the scalar primordial power spectrum. For example, as reported in PCI13, when a simple power law was generalized to allow for running, the bound on the tensor contribution degraded by approximately a factor of two. The new joint BICEP2/Keck Array-*Planck* upper bound (see Sect. 13), however, is much more robust and cannot be avoided by postulating baroque models that alter the scale dependence of the scalar power spectrum.

3. Methodology

This section describes updates to the formalism used to describe cosmological models and the likelihoods used with respect to the *Planck* 2013 inflation paper (PCI13).

3.1. Cosmological model

The cosmological models that predict observables such as the CMB anisotropies rely on inputs specifying the conditions and physics at play during different epochs of the history of the Universe. The primordial inputs describe the power spectrum of the cosmological perturbations at a time when all the observable modes were situated outside the Hubble radius. The inputs from this epoch consist of the primordial power spectra, which may include scalar curvature perturbations, tensor perturbations, and possibly also isocurvature modes and their correlations. The late time (i.e., $z \lesssim 10^4$) cosmological inputs include parameters such as $\omega_{\rm b}$, $\omega_{\rm c}$, Ω_Λ, and τ, which determine the conditions when the primordial perturbations become imprinted on the CMB and also the evolution of the Universe between last scattering and today, affecting primarily the angular diameter distance. Finally, there is a so-called "nuisance" component, consisting of parameters that determine how the measured CMB spectra are contaminated by unsubtracted Galactic and extragalactic foreground contamination. The focus of this paper is on the primordial inputs and how they are constrained by the observed CMB anisotropy, but we cannot completely ignore the other non-primordial parameters because their presence and uncertainties must be dealt with in order to correctly extract the primordial information of interest here.

As in PCI13, we adopt the minimal six-parameter spatially flat base ΛCDM cosmological model as our baseline for the late time cosmology, mainly altering the primordial inputs, i.e., the simple power-law spectrum parameterized by the scalar amplitude and spectral index for the adiabatic growing mode, which in this minimal model is the only late time mode excited. This model has four free non-primordial cosmological parameters ($\omega_{\rm b}, \omega_{\rm c}, \theta_{\rm MC}, \tau$; for a more detailed account of this model, we refer the reader to Planck Collaboration XIII 2016). On occasion, this assumption will be relaxed in order to consider the impact of more complex alternative late time cosmologies on our conclusions about inflation. Some of the commonly used cosmological parameters are defined in Table 1.

3.2. Primordial spectra of cosmological fluctuations

In inflationary models, comoving curvature ($\mathcal{R}$) and tensor (h) fluctuations are amplified by the nearly exponential expansion from quantum vacuum fluctuations to become highly squeezed states resembling classical states. Formally, this quantum mechanical phenomenon is most simply described by the evolution in conformal time, η, of the mode functions for

Table 1. Primordial, baseline, and optional late-time cosmological parameters.

Parameter	Definition
A_s	Scalar power spectrum amplitude (at $k_* = 0.05\,\mathrm{Mpc}^{-1}$)
n_s	Scalar spectral index (at $k_* = 0.05\,\mathrm{Mpc}^{-1}$ unless otherwise stated)
$\mathrm{d}n_s/\mathrm{d}\ln k$	Running of scalar spectral index (at $k_* = 0.05\,\mathrm{Mpc}^{-1}$ unless otherwise stated)
$\mathrm{d}^2n_s/\mathrm{d}\ln k^2$	Running of running of scalar spectral index (at $k_* = 0.05\,\mathrm{Mpc}^{-1}$)
r	Tensor-to-scalar power ratio (at $k_* = 0.05\,\mathrm{Mpc}^{-1}$ unless otherwise stated)
n_t	Tensor spectrum spectral index (at $k_* = 0.05\,\mathrm{Mpc}^{-1}$)
$\omega_b \equiv \Omega_b h^2$	Baryon density today
$\omega_c \equiv \Omega_c h^2$	Cold dark matter density today
θ_{MC}	Approximation to the angular size of sound horizon at last scattering
τ	Thomson scattering optical depth of reionized intergalactic medium
N_{eff}	Effective number of massive and massless neutrinos
Σm_ν	Sum of neutrino masses
Y_P	Fraction of baryonic mass in primordial helium
Ω_K	Spatial curvature parameter
w_{de}	Dark energy equation of state parameter (i.e., p_{de}/ρ_{de}) (assumed constant)

the gauge-invariant inflaton fluctuation, $\delta\phi$, and for the tensor fluctuation, h:

$$(ay_k)'' + \left(k^2 - \frac{x''}{x}\right) ay_k = 0, \tag{4}$$

with $(x, y) = (a\dot{\phi}/H, \delta\phi)$ for scalars and $(x, y) = (a, h)$ for tensors. Here a is the scale factor, primes indicate derivatives with respect to η, and $\dot{\phi}$ and $H = \dot{a}/a$ are the proper time derivative of the inflaton and the Hubble parameter, respectively. The curvature fluctuation, $\mathcal{R}$, and the inflaton fluctuation, $\delta\phi$, are related via $\mathcal{R} = H\delta\phi/\dot{\phi}$. Analytic and numerical calculations of the predictions for the primordial spectra of cosmological fluctuations generated during inflation have reached high standards of precision, which are more than adequate for our purposes, and the largest uncertainty in testing specific inflationary models arises from our lack of knowledge of the history of the Universe between the end of inflation and the present time, during the so-called "epoch of entropy generation".

This paper uses three different methods to compare inflationary predictions with *Planck* data. The first method consists of a phenomenological parameterization of the primordial spectra of scalar and tensor perturbations according to:

$$\begin{aligned}\mathcal{P}_\mathcal{R}(k) &= \frac{k^3}{2\pi^2}|\mathcal{R}_k|^2 \\ &= A_s \left(\frac{k}{k_*}\right)^{n_s - 1 + \frac{1}{2}\frac{\mathrm{d}n_s}{\mathrm{d}\ln k}\ln(k/k_*) + \frac{1}{6}\frac{\mathrm{d}^2 n_s}{\mathrm{d}\ln k^2}(\ln(k/k_*))^2 + \ldots},\end{aligned} \tag{5}$$

$$\mathcal{P}_t(k) = \frac{k^3}{2\pi^2}\left(|h_k^+|^2 + |h_k^\times|^2\right) = A_t \left(\frac{k}{k_*}\right)^{n_t + \frac{1}{2}\frac{\mathrm{d}n_t}{\mathrm{d}\ln k}\ln(k/k_*) + \ldots}, \tag{6}$$

where A_s (A_t) is the scalar (tensor) amplitude and n_s (n_t), $\mathrm{d}n_s/\mathrm{d}\ln k$ ($\mathrm{d}n_t/\mathrm{d}\ln k$), and $\mathrm{d}^2n_s/\mathrm{d}\ln k^2$ are the scalar (tensor) spectral index, the running of the scalar (tensor) spectral index, and the running of the running of the scalar spectral index, respectively. $h^{+,\times}$ denotes the amplitude of the two polarization states $(+, \times)$ of gravitational waves and k_* is the pivot scale. Unless otherwise stated, the tensor-to-scalar ratio,

$$r = \frac{\mathcal{P}_t(k_*)}{\mathcal{P}_\mathcal{R}(k_*)}, \tag{7}$$

is fixed to $-8n_t$, which is the relation that holds when inflation is driven by a single slow-rolling scalar field with a standard kinetic term[2]. We will use a parameterization analogous to Eq. (5) with no running for the power spectra of isocurvature modes and their correlations in Sect. 11.

The second method exploits the analytic dependence of the slow-roll power spectra of primordial perturbations in Eqs. (5) and (6) on the values of the Hubble parameter and the hierarchy of its time derivatives, known as the Hubble flow functions (HFF): $\epsilon_1 = -\dot{H}/H^2$, $\epsilon_{i+1} \equiv \dot{\epsilon}_i/(H\epsilon_i)$, with $i \geq 1$. We will use the analytic power spectra calculated up to second order using the Green's function method (Gong & Stewart 2001; Leach et al. 2002; see Habib et al. 2002; Martin & Schwarz 2003; and Casadio et al. 2006 for alternative derivations). The spectral indices and the relative scale dependence in Eqs. (5) and (6) are given in terms of the HFFs by:

$$n_s - 1 = -2\epsilon_1 - \epsilon_2 - 2\epsilon_1^2 - (2C + 3)\,\epsilon_1\,\epsilon_2 - C\epsilon_2\epsilon_3, \tag{8}$$

$$\mathrm{d}n_s/\mathrm{d}\ln k = -2\epsilon_1\epsilon_2 - \epsilon_2\epsilon_3, \tag{9}$$

$$n_t = -2\epsilon_1 - 2\epsilon_1^2 - 2\,(C + 1)\,\epsilon_1\,\epsilon_2, \tag{10}$$

$$\mathrm{d}n_t/\mathrm{d}\ln k = -2\epsilon_1\epsilon_2, \tag{11}$$

where $C \equiv \ln 2 + \gamma_E - 2 \approx -0.7296$ (γ_E is the Euler-Mascheroni constant). See the Appendix of PCI13 for more details. Primordial spectra as functions of the ϵ_i will be employed in Sect. 6, and the expressions generalizing Eqs. (8) to (11) for a general Lagrangian $p(\phi, X)$, where $X \equiv -g^{\mu\nu}\partial_\mu\phi\partial_\nu\phi/2$, will be used in Sect. 10. The good agreement between the first and second method as well as with alternative approximations of slow-roll spectra is illustrated in the Appendix of PCI13.

The third method is fully numerical, suitable for models where the slow-roll conditions are not well satisfied and analytical approximations for the primordial fluctuations are not available. Two different numerical codes, the inflation module of Lesgourgues & Valkenburg (2007) as implemented in `CLASS` (Lesgourgues 2011; Blas et al. 2011) and `ModeCode` (Adams et al. 2001; Peiris et al. 2003; Mortonson et al. 2009; Easther & Peiris 2012), are used in Sects. 7 and 10, respectively.[3]

Conventions for the functions and symbols used to describe inflationary physics are defined in Table 2.

[2] When running is considered, we fix $n_t = -r(2 - r/8 - n_s)/8$ and $\mathrm{d}n_t/\mathrm{d}\ln k = r(r/8 + n_s - 1)/8$.

[3] `http://class-code.net`, `http://modecode.org`

Table 2. Conventions and definitions for inflation physics.

Parameter	Definition
ϕ	Inflaton
$V(\phi)$	Inflaton potential
a	Scale factor
t	Cosmic (proper) time
δX	Fluctuation of X
$\dot{X} = \mathrm{d}X/\mathrm{d}t$	Derivative with respect to proper time
$X' = \mathrm{d}X/\mathrm{d}\eta$	Derivative with respect to conformal time
$X_\phi = \partial X/\partial\phi$	Partial derivative with respect to ϕ
$M_{\rm pl}$	Reduced Planck mass ($=2.435\times10^{18}$ GeV)
$\mathcal{R}$	Comoving curvature perturbation
$h^{+,\times}$	Gravitational wave amplitude of $(+,\times)$-polarization component
X_*	X evaluated at Hubble exit during inflation of mode with wavenumber k_*
$X_{\rm e}$	X evaluated at end of inflation
$\epsilon_V = M_{\rm pl}^2 V_\phi^2/(2V^2)$	First slow-roll parameter for $V(\phi)$
$\eta_V = M_{\rm pl}^2 V_{\phi\phi}/V$	Second slow-roll parameter for $V(\phi)$
$\xi_V^2 = M_{\rm pl}^4 V_\phi V_{\phi\phi\phi}/V^2$	Third slow-roll parameter for $V(\phi)$
$\varpi_V^3 = M_{\rm pl}^6 V_\phi^2 V_{\phi\phi\phi\phi}/V^3$	Fourth slow-roll parameter for $V(\phi)$
$\epsilon_1 = -\dot{H}/H^2$	First Hubble hierarchy parameter
$\epsilon_{n+1} = \dot{\epsilon}_n/(H\epsilon_n)$	$(n+1)$st Hubble hierarchy parameter (where $n \geq 1$)
$N(t) = \int_t^{t_{\rm e}} \mathrm{d}t\, H$	Number of e-folds to end of inflation

3.3. Planck data

The *Planck* data processing proceeding from time-ordered data to maps has been improved for this 2015 release in various aspects (Planck Collaboration II 2016; Planck Collaboration VII 2016). We refer the interested reader to Planck Collaboration II (2016) and Planck Collaboration VII (2016) for details, and we describe here two of these improvements. The absolute calibration has been improved using the orbital dipole and more accurate characterization of the *Planck* beams. The calibration discrepancy between *Planck* and WMAP described in Planck Collaboration XXXI (2014) for the 2013 release has now been greatly reduced. At the time of that release, a blind analysis for primordial power spectrum reconstruction described a broad feature at $\ell \approx 1800$ in the temperature power spectrum, which was most prominent in the 217×217 GHz auto-spectra (PCI13). In work done after the *Planck* 2013 data release, this feature was shown to be associated with imperfectly subtracted systematic effects associated with the 4 K cooler lines, which were particularly strong in the first survey. This systematic effect was shown to potentially lead to 0.5σ shifts in the cosmological parameters, slightly increasing $n_{\rm s}$ and H_0, similarly to the case in which the 217×217 channel was excised from the likelihood (Planck Collaboration XV 2014; Planck Collaboration XVI 2014). The *Planck* likelihood (Planck Collaboration XI 2016) is based on the full mission data and comprises temperature and polarization data (see Fig. 2).

Planck low-ℓ likelihood

The *Planck* low-ℓ temperature-polarization likelihood uses foreground-cleaned LFI 70 GHz polarization maps together with the temperature map obtained from the *Planck* 30 to 353 GHz channels by the `Commander` component separation algorithm over 94% of the sky (see Planck Collaboration IX 2016 for further details). The *Planck* polarization map uses the LFI 70 GHz (excluding Surveys 2 and 4) low-resolution maps of Q and U polarization from which polarized synchrotron and thermal dust emission components have been removed using the LFI 30 GHz and HFI 353 GHz maps as templates, respectively. (See Planck Collaboration XI 2016 for more details.) The polarization map covers the 46% of the sky outside the lowP polarization mask.

The low-ℓ likelihood is pixel-based and treats the temperature and polarization at the same resolution of 3.°6, or `HEALpix` (Górski et al. 2005) $N_{\rm side} = 16$. Its multipole range extends from $\ell = 2$ to $\ell = 29$ in *TT*, *TE*, *EE*, and *BB*. In the 2015 *Planck* papers the polarization part of this likelihood is denoted as "lowP".[4] This *Planck* low-ℓ likelihood replaces the *Planck* temperature low-ℓ Gibbs module combined with the WMAP 9-yr low-ℓ polarization module used in the *Planck* 2013 cosmology papers (denoted by WP), which used lower resolution polarization maps at $N_{\rm side} = 8$ (about 7.°3). With this *Planck*-only low-ℓ likelihood module, the basic *Planck* results presented in this release are completely independent of external information.

The *Planck* low-multipole likelihood alone implies $\tau = 0.067 \pm 0.022$ (Planck Collaboration XI 2016), a value smaller than the value inferred using the WP polarization likelihood, $\tau = 0.089 \pm 0.013$, used in the *Planck* 2013 papers (Planck Collaboration XV 2014). See Planck Collaboration XIII (2016) for the important implications of this decrease in τ for reionization. However, the LFI 70 GHz and WMAP polarization maps are in very good agreement when both are foreground-cleaned

[4] In this paper we use the conventions introduced in Planck Collaboration XIII (2016). We adopt the following labels for likelihoods: (i) *Planck* TT denotes the combination of the *TT* likelihood at multipoles $\ell \geq 30$ and a low-ℓ temperature-only likelihood based on the CMB map recovered with `Commander`; (ii) *Planck* TT–lowT denotes the *TT* likelihood at multipoles $\ell \geq 30$; (iii) *Planck* TT+lowP further includes the *Planck* polarization data in the low-ℓ likelihood, as described in the main text; (iv) *Planck TE* denotes the likelihood at $\ell \geq 30$ using the *TE* spectrum; and (v) *Planck* TT, TE, EE+lowP denotes the combination of the likelihood at $\ell \geq 30$ using *TT*, *TE*, and *EE* spectra and the low-ℓ multipole likelihood. The label "τ prior" denotes the use of a Gaussian prior $\tau = 0.07 \pm 0.02$. The labels "lowT, P" and "lowEB" denote the low-ℓ multipole likelihood and the Q, U pixel likelihood only, respectively.

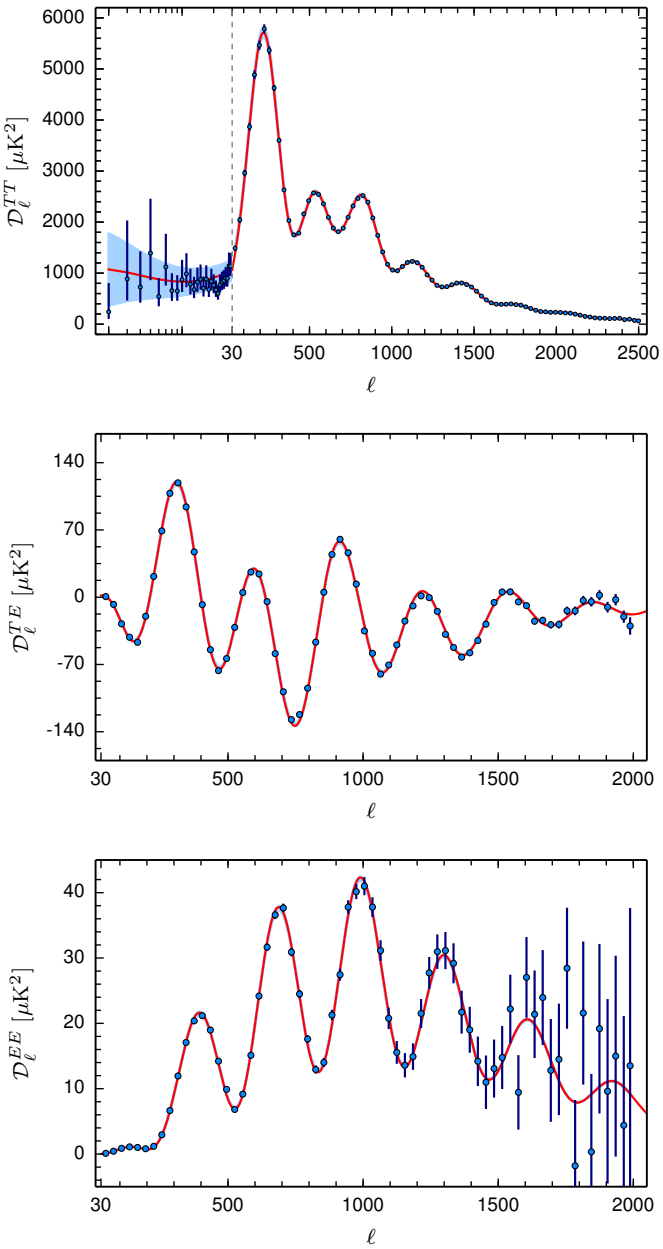

Fig. 2. *Planck TT* (*top*), high-ℓ *TE* (*centre*), and high-ℓ *EE* (*bottom*) angular power spectra. Here $\mathcal{D}_\ell \equiv \ell(\ell+1)C_\ell/(2\pi)$.

using the HFI 353 GHz map as a polarized dust template (see Planck Collaboration XI 2016 for further details). Therefore, it is useful to construct a noise-weighted combination to obtain a joint *Planck*/WMAP low resolution polarization data set, also described in Planck Collaboration XI (2016), using as a polarization mask the union of the WMAP P06 and *Planck* lowP polarization masks and keeping 74% of the sky. The polarization part of the combined low multipole likelihood is called lowP+WP. This combined low multipole likelihood gives $\tau = 0.071^{+0.011}_{-0.013}$ (Planck Collaboration XI 2016).

Planck high-ℓ likelihood

Following Planck Collaboration XV (2014), and Planck Collaboration XI 2016 for polarization, we use a Gaussian approximation for the high-ℓ part of the likelihood ($30 < \ell < 2500$), so that

$$-\log\mathcal{L}\big(\hat{C}|C(\boldsymbol{\theta})\big) = \frac{1}{2}\big(\hat{C} - C(\boldsymbol{\theta})\big)^T \mathcal{M}^{-1}\big(\hat{C} - C(\boldsymbol{\theta})\big), \tag{12}$$

where a constant offset has been discarded. Here $\hat{C}$ is the data vector, $C(\boldsymbol{\theta})$ is the model prediction for the parameter value vector $\boldsymbol{\theta}$, and $\mathcal{M}$ is the covariance matrix. For the data vector, we use 100 GHz, 143 GHz, and 217 GHz half-mission cross-power spectra, avoiding the Galactic plane as well as the brightest point sources and the regions where the CO emission is the strongest. We retain 66% of the sky for 100 GHz, 57% for 143 GHz, and 47% for 217 GHz for the T masks, and respectively 70%, 50%, and 41% for the Q, U masks. Following Planck Collaboration XXX (2014), we do not mask for any other Galactic polarized emission. All the spectra are corrected for the beam and pixel window functions using the same beam for temperature and polarization. (For details see Planck Collaboration XI 2016.)

The model for the cross-spectra can be written as

$$C_{\mu,\nu}(\theta) = \frac{C^{\rm cmb}(\theta) + C^{\rm fg}_{\mu,\nu}(\theta)}{\sqrt{c_\mu c_\nu}}, \tag{13}$$

where $C^{\rm cmb}(\theta)$ is the CMB power spectrum, which is independent of the frequency, $C^{fg}_{\mu,\nu}(\theta)$ is the foreground model contribution for the cross-frequency spectrum $\mu \times \nu$, and c_μ is the calibration factor for the $\mu \times \mu$ spectrum. The model for the foreground residuals includes the following components: Galactic dust, clustered cosmic infrared background (CIB), thermal and kinetic Sunyaev-Zeldovich (tSZ and kSZ) effect, tSZ correlations with CIB, and point sources, for the TT foreground modeling; and for polarization, only dust is included. All the components are modelled by smooth C_ℓ templates with free amplitudes, which are determined along with the cosmological parameters as the likelihood is explored. The tSZ and kSZ models are the same as in 2013 (see Planck Collaboration XV 2014), although with different priors (Planck Collaboration XI 2016; Planck Collaboration XIII 2016), while the CIB and tSZ-CIB correlation models use the updated CIB models described in Planck Collaboration XXX (2014). The point source contamination is modelled as Poisson noise with an independent amplitude for each frequency pair. Finally, the dust contribution uses an effective smooth model measured from high frequency maps. Details of our dust and noise modelling can be found in Planck Collaboration XI (2016). The dust is the dominant foreground component for TT at $\ell < 500$, while the point source component, and for 217×217 also the CIB component, dominate at high ℓ. The other foreground components are poorly determined by *Planck*. Finally, our treatment of the calibration factors and beam uncertainties and mismatch are described in Planck Collaboration XI (2016).

The covariance matrix accounts for the correlation due to the mask and is computed following the equations in Planck Collaboration XV (2014), extended to polarization in Planck Collaboration XI (2016) and references therein. The fiducial model used to compute the covariance is based on a joint fit of base ΛCDM and nuisance parameters obtained with a previous version of the matrix. We iterate the process until the parameters stop changing. For more details, see Planck Collaboration XI (2016).

The joint unbinned covariance matrix is approximately of size $23\,000 \times 23\,000$. The memory and speed requirements for dealing with such a huge matrix are significant, so to reduce its

size, we bin the data and the covariance matrix to compress the data vector size by a factor of 10. The binning uses varying bin width with $\Delta\ell = 5$ for $29 < \ell < 100$, $\Delta\ell = 9$ for $99 < \ell < 1504$, $\Delta\ell = 17$ for $1503 < \ell < 2014$, and $\Delta\ell = 33$ for $2013 < \ell < 2509$, and a weighting in $\ell(\ell+1)$ to flatten the spectrum. Where a higher resolution is desirable, we also use a more finely binned version ("bin3", unbinned up to $\ell = 80$ and $\Delta\ell = 3$ beyond that) as well as a completely unbinned version ("bin1"). We use odd bin sizes, since for an azimuthally symmetric mask, the correlation between a multipole and its neighbours is symmetric, oscillating between positive and negative values. Using the base ΛCDM model and single-parameter classical extensions, we confirmed that the cosmological and nuisance parameter fits with or without binning are indistinguishable.

As discussed in Planck Collaboration XI (2016) and Planck Collaboration XIII (2016), the *TE* and *EE* high-ℓ data are not free of small systematic effects, such as leakage from temperature to polarization. Although the propagated effects of these residual systematics on cosmological parameters are small and do not alter the conclusions of this paper, we mainly refer to *Planck* TT+lowP in combination with the *Planck* lensing or additional data sets as the most reliable results for this release.

Planck CMB bispectrum

We use measurements of the non-Gaussianity amplitude $f_{\rm NL}$ from the CMB bispectrum presented in Planck Collaboration XVII (2016). Non-Gaussianity constraints have been obtained using three optimal bispectrum estimators: separable template fitting (also known as "KSW"), binned, and modal. The maps analysed are the *Planck* 2015 full mission sky maps, both in temperature and in *E* polarization, as cleaned with the four component separation methods SMICA, SEVEM, NILC, and Commander. The map is masked to remove the brightest parts of the Galaxy as well as the brightest point sources and covers approximately 70% of the sky. In this paper we mainly exploit the joint constraints on equilateral and orthogonal non-Gaussianity (after removing the integrated Sachs-Wolfe effect-lensing bias), $f_{\rm NL}^{\rm equil} = -16 \pm 70$, $f_{\rm NL}^{\rm ortho} = -34 \pm 33$ from *T* only, and $f_{\rm NL}^{\rm equil} = -3.7 \pm 43$, $f_{\rm NL}^{\rm ortho} = -26 \pm 21$ from *T* and *E* (68% CL). For reference, the constraints on local non-Gaussianity are $f_{\rm NL}^{\rm local} = 2.5 \pm 5.7$ from *T* only, and $f_{\rm NL}^{\rm local} = 0.8 \pm 5.0$ from *T* and *E* (68% CL). Starting from a Gaussian $f_{\rm NL}$-likelihood, which is an accurate assumption in the regime of small primordial non-Gaussianity, we use these constraints to derive limits on the sound speed of the inflaton fluctuations (or other microscopic parameters of inflationary models; Planck Collaboration XXIV 2014). The bounds on the sound speed for various models are then used in combination with *Planck* power spectrum data.

Planck CMB lensing data

Some of our analysis includes the *Planck* 2015 lensing likelihood, presented in Planck Collaboration XV (2016), which utilizes the non-Gaussian trispectrum induced by lensing to estimate the power spectrum of the lensing potential, $C_\ell^{\phi\phi}$. This signal is extracted using a full set of temperature- and polarization-based quadratic lensing estimators (Okamoto & Hu 2003) applied to the SMICA CMB map over approximately 70% of the sky, as described in Planck Collaboration IX (2016). We have used the conservative bandpower likelihood, covering multipoles $40 \le \ell \le 400$. This provides a measurement of the lensing potential power at the 40σ level, giving a 2.5%-accurate constraint on the overall lensing power in this multipole range. The measurement of the lensing power spectrum used here is approximately twice as powerful as the measurement used in our previous 2013 analysis (Planck Collaboration XXII 2014; Planck Collaboration XVII 2014), which used temperature-only data from the *Planck* nominal mission data set.

3.4. Non-*Planck* data

BAO data

Baryon acoustic oscillations (BAO) are the counterpart in the late time matter power spectrum of the acoustic oscillations seen in the CMB multipole spectrum (Eisenstein et al. 2005). Both originate from coherent oscillations of the photon-baryon plasma before these two components become decoupled at recombination. Measuring the position of these oscillations in the matter power spectra at different redshifts constrains the expansion history of the universe after decoupling, thus removing degeneracies in the interpretation of the CMB anisotropies.

In this paper, we combine constraints on $D_V(\bar{z})/r_{\rm s}$ (the ratio between the spherically-averaged distance scale D_V to the effective survey redshift, $\bar{z}$, and the sound horizon, $r_{\rm s}$) inferred from 6dFGRS data (Beutler et al. 2011) at $\bar{z} = 0.106$, the SDSS-MGS data (Ross et al. 2015) at $\bar{z} = 0.15$, and the SDSS-DR11 CMASS and LOWZ data (Anderson et al. 2014) at redshifts $\bar{z} = 0.57$ and 0.32. For details see Planck Collaboration XIII (2016).

Joint BICEP2/Keck Array and *Planck* constraint on *r*

Since the *Planck* temperature constraints on the tensor-to-scalar ratio are close to the cosmic variance limit, the inclusion of data sets sensitive to the expected *B*-mode signal of primordial gravitational waves is particularly useful. In this paper, we provide results including the joint analysis cross-correlating BICEP2/Keck Array observations and *Planck* (BKP). Combining the more sensitive BICEP2/Keck Array *B*-mode polarization maps in the approximately 400 deg^2 BICEP2 field with the *Planck* maps at higher frequencies where dust dominates allows a statistical analysis taking into account foreground contamination. Using *BB* auto- and cross-frequency spectra between BICEP2/Keck Array (150 GHz) and *Planck* (217 and 353 GHz), BKP find a 95% upper limit of $r_{0.05} < 0.12$.

3.5. Parameter estimation and model comparison

Much of this paper uses a Bayesian approach to parameter estimation, and unless otherwise specified, we assign broad top-hat prior probability distributions to the cosmological parameters listed in Table 1. We generate posterior probability distributions for the parameters using either the Metropolis-Hastings algorithm implemented in CosmoMC (Lewis & Bridle 2002) or MontePython (Audren et al. 2013), the nested sampling algorithm MultiNest (Feroz & Hobson 2008; Feroz et al. 2009, 2013), or PolyChord, which combines nested sampling with slice sampling (Handley et al. 2015). The latter two also compute the Bayesian evidence needed for model comparison. Nevertheless, χ^2 values are often provided as well (using CosmoMC's implementation of the BOBYQA algorithm (Powell 2009) for maximizing the likelihood), and other parts of the paper employ frequentist methods when appropriate.

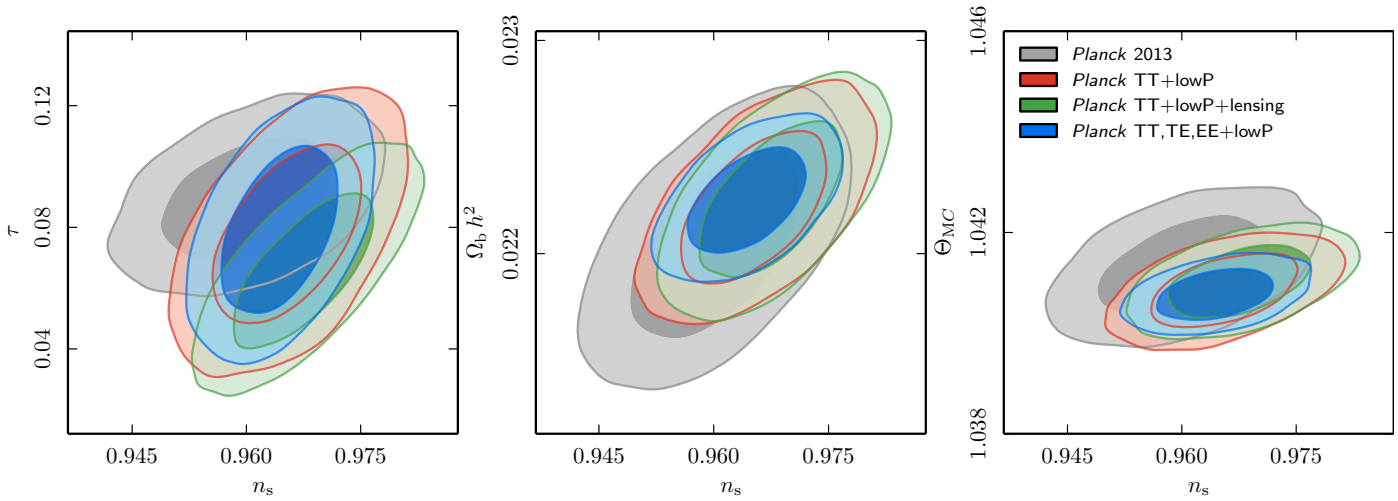

Fig. 3. Comparison of the marginalized joint 68% and 95% CL constraints on (n_s, τ) (*left panel*), $(n_s, \Omega_b h^2)$ (*middle panel*), and (n_s, θ_{MC}) (*right panel*), for *Planck* 2013 (grey contours), *Planck* TT+lowP (red contours), *Planck* TT+lowP+lensing (green contours), and *Planck* TT, TE, EE+lowP (blue contours).

Table 3. Confidence limits on the parameters of the base ΛCDM model, for various combinations of *Planck* 2015 data, at the 68% confidence level.

Parameter	TT+lowP	TT+lowP+lensing	TT+lowP+BAO	TT, TE, EE+lowP
$\Omega_b h^2$	0.02222 ± 0.00023	0.02226 ± 0.00023	0.02226 ± 0.00020	0.02225 ± 0.00016
$\Omega_c h^2$	0.1197 ± 0.0022	0.1186 ± 0.0020	0.1190 ± 0.0013	0.1198 ± 0.0015
$100\theta_{MC}$	1.04085 ± 0.00047	1.04103 ± 0.00046	1.04095 ± 0.00041	1.04077 ± 0.00032
τ	0.078 ± 0.019	0.066 ± 0.016	0.080 ± 0.017	0.079 ± 0.017
$\ln(10^{10} A_s)$	3.089 ± 0.036	3.062 ± 0.029	3.093 ± 0.034	3.094 ± 0.034
n_s	0.9655 ± 0.0062	0.9677 ± 0.0060	0.9673 ± 0.0045	0.9645 ± 0.0049
H_0	67.31 ± 0.96	67.81 ± 0.92	67.63 ± 0.57	67.27 ± 0.66
Ω_m	0.315 ± 0.013	0.308 ± 0.012	0.3104 ± 0.0076	0.3156 ± 0.0091

4. Constraints on the primordial spectrum of curvature perturbations

One of the most important results of the *Planck* nominal mission was the determination of the departure from scale invariance for the spectrum of scalar perturbations at high statistical significance (Planck Collaboration XVI 2014; Planck Collaboration XXII 2014). We now update these measurements with the *Planck* full mission data in temperature and polarization.

4.1. Tilt of the curvature power spectrum

For the base ΛCDM model with a power-law power spectrum of curvature perturbations, the constraint on the scalar spectral index, n_s, with the *Planck* full mission temperature data is

$$n_s = 0.9655 \pm 0.0062 \text{ (68\% CL, } \textit{Planck} \text{ TT+lowP).} \quad (14)$$

This result is compatible with the *Planck* 2013 constraint, $n_s = 0.9603 \pm 0.0073$ (Planck Collaboration XV 2014; Planck Collaboration XVI 2014). See Fig. 3 for the accompanying changes in τ, $\Omega_b h^2$, and θ_{MC}. The shift towards higher values for n_s with respect to the nominal mission results is due to several improvements in the data processing and likelihood which are discussed in Sect. 3, including the removal of the 4 K cooler systematics. For the values of other cosmological parameters in the base ΛCDM model, see Table 3. We also provide the results for the base ΛCDM model and extended models online.[5]

When the *Planck* high-ℓ polarization is combined with temperature, we obtain

$$n_s = 0.9645 \pm 0.0049 \text{ (68\% CL, } \textit{Planck} \text{ TT, TE, EE+lowP),} \quad (15)$$

together with $\tau = 0.079 \pm 0.017$ (68% CL), which is consistent with the TT+lowP results. The *Planck* high-ℓ polarization pulls τ up to a slightly higher value. When the *Planck* lensing measurement is added to the temperature data, we obtain

$$n_s = 0.9677 \pm 0.0060 \text{ (68\% CL, } \textit{Planck} \text{ TT+lowP+lensing),} \quad (16)$$

with $\tau = 0.066 \pm 0.016$ (68% CL). The shift towards slightly smaller values of the optical depth is driven by a marginal preference for a smaller primordial amplitude, A_s, in the *Planck* lensing data (Planck Collaboration XV 2016). Given that the temperature data provide a sharp constraint on the combination $e^{-2\tau} A_s$, a slightly lower A_s requires a smaller optical depth to reionization.

4.2. Viability of the Harrison-Zeldovich spectrum

Even though the estimated scalar spectral index has risen slightly with respect to the *Planck* 2013 release, the assumption of

[5] http://www.cosmos.esa.int/web/planck/pla

a Harrison-Zeldovich (HZ) scale-invariant spectrum (Harrison 1970; Peebles & Yu 1970; Zeldovich 1972) continues to be disfavoured (with a modest increase in significance, from 5.1σ in 2013 to 5.6σ today), because the error bar on n_s has decreased. The value of n_s inferred from the *Planck* 2015 temperature plus large-scale polarization data lies 5.6 standard deviations away from unity (with a corresponding $\Delta\chi^2 = 29.9$), if one assumes the base ΛCDM late-time cosmological model. If we consider more general reionization models, parameterized by a principal component analysis (Mortonson & Hu 2008) instead of τ (where reionization is assumed to have occurred instantaneously), we find $\Delta\chi^2 = 14.9$ for $n_s = 1$. Previously, simple one-parameter extensions of the base model, such as ΛCDM+$N_{\rm eff}$ (where $N_{\rm eff}$ is the effective number of neutrino flavours) or ΛCDM+$Y_{\rm P}$ (where $Y_{\rm P}$ is the primordial value of the helium mass fraction), could nearly reconcile the *Planck* temperature data with $n_s = 1$. They now lead to $\Delta\chi^2 = 7.6$ and 9.3, respectively. For any of the cosmological models that we have considered, the $\Delta\chi^2$ by which the HZ model is penalized with respect to the tilted model has increased since the 2013 analysis (PCI13) thanks to the constraining power of the full mission temperature data. Adding *Planck* high-ℓ polarization data further disfavours the HZ model: in ΛCDM, the χ^2 increases by 57.8, for general reionization we obtain $\Delta\chi^2 = 41.3$, and for ΛCDM+$N_{\rm eff}$ and ΛCDM+$Y_{\rm P}$ we find $\Delta\chi^2 = 22.5$ and 24.0, respectively.

4.3. Running of the spectral index

The running of the scalar spectral index is constrained by the *Planck* 2015 full mission temperature data to

$$\frac{{\rm d}n_s}{{\rm d}\ln k} = -0.0084 \pm 0.0082 \ (68\%\ {\rm CL},\ \textit{Planck}\ {\rm TT{+}lowP}). \quad (17)$$

The combined constraint including high-ℓ polarization is

$$\frac{{\rm d}n_s}{{\rm d}\ln k} = -0.0057 \pm 0.0071 \ (68\%\ {\rm CL},\ \textit{Planck}\ {\rm TT,\ TE,\ EE{+}lowP}). \quad (18)$$

Adding the *Planck* CMB lensing data to the temperature data further reduces the central value for the running, i.e., ${\rm d}n_s/{\rm d}\ln k = -0.0033 \pm 0.0074$ (68% CL, *Planck* TT+lowP+lensing).

The central value for the running has decreased in magnitude with respect to the *Planck* 2013 nominal mission (Planck Collaboration XVI 2014 found ${\rm d}n_s/{\rm d}\ln k = -0.013 \pm 0.009$; see Fig. 4), and the improvement of the maximum likelihood with respect to a power-law spectrum is smaller, $\Delta\chi^2 \approx -0.8$. Among the different effects contributing to the decrease in the central value of the running with respect to the *Planck* 2013 result, we mention a change in HFI beams at $\ell \lesssim 200$ (Planck Collaboration XIII 2016). Nevertheless, the deficit of power at low multipoles in the *Planck* 2015 temperature power spectrum contributes to a preference for slightly negative values of the running, but with low statistical significance.

The *Planck* constraints on n_s and ${\rm d}n_s/{\rm d}\ln k$ are remarkably stable against the addition of the BAO likelihood. The combination with BAO shifts n_s to slighly higher values and shrinks its uncertainty by about 30% when only high-ℓ temperature is considered, and by only about 15% when high-ℓ temperature and polarization are combined. In slow-roll inflation, the running of the scalar spectral index is connected to the third derivative of the potential (Kosowsky & Turner 1995). As was the case for the nominal mission results, values of the running compatible with the *Planck* 2015 constraints can be obtained in viable inflationary models (Kobayashi & Takahashi 2011).

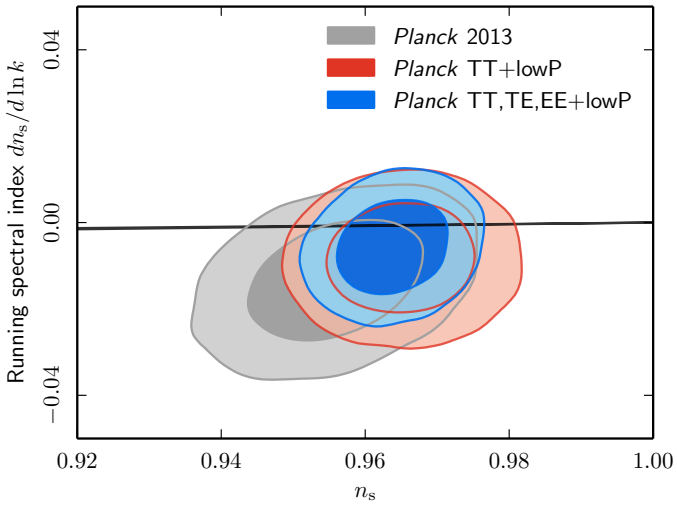

Fig. 4. Marginalized joint 68% and 95% CL for $(n_s, {\rm d}n_s/{\rm d}\ln k)$ using *Planck* TT+lowP and *Planck* TT, TE, EE+lowP. Constraints from the Planck 2013 data release are also shown for comparison. For comparison, the thin black stripe shows the prediction for single-field monomial chaotic inflationary models with $50 < N_* < 60$.

When the running of the running is allowed to float, the *Planck* TT+lowP (*Planck* TT, TE, EE+lowP) data give:

$$n_s = 0.9569 \pm 0.0077 \ \ (0.9586 \pm 0.0056),$$
$${\rm d}n_s/{\rm d}\ln k = 0.011^{+0.014}_{-0.013} \ \ (0.009 \pm 0.010), \quad (68\%\ {\rm CL}) \quad (19)$$
$${\rm d}^2 n_s/{\rm d}\ln k^2 = 0.029^{+0.015}_{-0.016} \ \ (0.025 \pm 0.013),$$

at the pivot scale $k_* = 0.05\,{\rm Mpc}^{-1}$. Allowing for running of the running provides a better fit to the temperature spectrum at low multipoles, such that $\Delta\chi^2 \approx -4.8$ (−4.9) for TT+lowP (TT, TE, EE+lowP), but is not statistically preferred over the simplest ΛCDM model.

Note that the inclusion of small-scale data such as Lyα might further constrain the running of the spectral index and its derivative. The recent analysis of the BOSS one-dimensional Lyα flux power spectrum presented in Palanque-Delabrouille et al. (2015) and Rossi et al. (2015) was optimized for measuring the neutrino mass. It does not include constraints on the spectral index running, which would require new dedicated N-body simulations. Hence we do not include Lyα constraints here.

In Sect. 7 on inflaton potential reconstruction we will show that the data cannot accomodate a significant running but are compatible with a larger running of the running.

4.4. Suppression of power on the largest scales

Although not statistically significant, the trend for a negative running or positive running of the running observed in the last subsection was driven by the lack of power in the *Planck* temperature power spectrum at low multipoles, already mentioned in the *Planck* 2013 release. This deficit could potentially be explained by a primordial spectrum featuring a depletion of power *only* at large wavelengths. Here we investigate two examples of such models.

Table 4. Constraints on the primordial perturbation parameters for ΛCDM+r and ΛCDM+r+dn_s/dln k models from *Planck*.

Model	Parameter	*Planck* TT+lowP	*Planck* TT+lowP+lensing	*Planck* TT+lowP+BAO	*Planck* TT, TE, EE+lowP
ΛCDM+r	n_s	0.9666 ± 0.0062	0.9688 ± 0.0061	0.9680 ± 0.0045	0.9652 ± 0.0047
	$r_{0.002}$	<0.103	<0.114	<0.113	<0.099
	$-2\Delta \ln \mathcal{L}_{\max}$	0	0	0	0
ΛCDM+r +dn_s/dln k	n_s	0.9667 ± 0.0066	0.9690 ± 0.0063	0.9673 ± 0.0043	0.9644 ± 0.0049
	$r_{0.002}$	<0.180	<0.186	<0.176	<0.152
	r	<0.168	<0.176	<0.166	<0.149
	dn_s/dln k	$-0.0126^{+0.0098}_{-0.0087}$	$-0.0076^{+0.0092}_{-0.0080}$	−0.0125 ± 0.0091	−0.0085 ± 0.0076
	$-2\Delta \ln \mathcal{L}_{\max}$	−0.81	−0.08	−0.87	−0.38

Notes. Constraints on the spectral index and its dependence on the wavelength are given at the pivot scale of $k_* = 0.05$ Mpc^{-1}.

We first update the analysis (already presented in PCI13) of a power-law spectrum multiplied by an exponential cutoff:

$$\mathcal{P}_{\mathcal{R}}(k) = \mathcal{P}_0(k)\left\{1 - \exp\left[-\left(\frac{k}{k_c}\right)^{\lambda_c}\right]\right\}. \quad (20)$$

This simple parameterization is motivated by models with a short inflationary stage in which the onset of the slow-roll phase coincides with the time when the largest observable scales exited the Hubble radius during inflation. The curvature spectrum is then strongly suppressed on those scales. We apply top-hat priors on the parameter λ_c, controlling the steepness of the cutoff, and on the logarithm of the cutoff scale, k_c. We choose prior ranges $\lambda_c \in [0, 10]$ and $\ln(k_c/\mathrm{Mpc}^{-1}) \in [-12, -3]$. For *Planck* TT+lowP (*Planck* TT, TE, EE+lowP), the best-fit model has $\lambda_c = 0.50\,(0.53)$, $\ln(k_c/\mathrm{Mpc}^{-1}) = -7.98\ (-7.98)$, $n_s = 0.9647\ (0.9649)$, and improves the effective χ^2 by a modest amount, $\Delta\chi^2 \approx -3.4\ (-3.4)$.

As a second model, we consider a broken power-law spectrum for curvature perturbations:

$$\mathcal{P}_{\mathcal{R}}(k) = \begin{cases} A_{\rm low}\left(\frac{k}{k_*}\right)^{n_s-1+\delta} & \text{if } k \le k_b, \\ A_s\left(\frac{k}{k_*}\right)^{n_s-1} & \text{if } k \ge k_b, \end{cases} \quad (21)$$

with $A_{\rm low} = A_s(k_b/k_*)^{-\delta}$ to ensure continuity at $k = k_b$. Hence this model, like the previous one, has two parameters, and also suppresses power at large wavelengths when $\delta > 0$. We assume top-hat priors $\delta \in [0, 2]$ and $\ln(k_b/\mathrm{Mpc}^{-1}) \in [-12, -3]$, and standard uniform priors for $\ln(10^{10}A_s)$ and n_s. The best fit to *Planck* TT+lowP (*Planck* TT, TE, EE+lowP) is found for $n_s = 0.9658\ (0.9647)$, $\delta = 1.14\ (1.14)$, and $\ln(k_b/\mathrm{Mpc}^{-1}) = -7.55\ (-7.57)$, with a very small χ^2 improvement of $\Delta\chi^2 \approx -1.9\,(-1.6)$.

We conclude that neither of these two models with two extra parameters is preferred over the base ΛCDM model. (See also the discussion of a step inflationary potential in Sect. 9.1.1.)

5. Constraints on tensor modes

In this section, we focus on the *Planck* 2015 constraints on tensor perturbations. Unless otherwise stated, we consider that the tensor spectral index satisfies the standard inflationary consistency condition to lowest order in slow roll, $n_t = -r/8$. We recall that r is defined at the pivot scale $k_* = 0.05\,\mathrm{Mpc}^{-1}$. However, for comparison with other studies, we also report our bounds in terms of the tensor-to-scalar ratio $r_{0.002}$ at $k_* = 0.002\,\mathrm{Mpc}^{-1}$.

5.1. *Planck* 2015 upper bound on r

The constraints on the tensor-to-scalar ratio inferred from the *Planck* full mission data for the ΛCDM+r model are:

$$r_{0.002} < 0.10 \quad (95\%\ \mathrm{CL}, \textit{Planck}\ \mathrm{TT+lowP}), \quad (22)$$
$$r_{0.002} < 0.11 \quad (95\%\ \mathrm{CL}, \textit{Planck}\ \mathrm{TT+lowP+lensing}), \quad (23)$$
$$r_{0.002} < 0.11 \quad (95\%\ \mathrm{CL}, \textit{Planck}\ \mathrm{TT+lowP+BAO}), \quad (24)$$
$$r_{0.002} < 0.10 \quad (95\%\ \mathrm{CL}, \textit{Planck}\ \mathrm{TT, TE, EE+lowP}). \quad (25)$$

Table 4 also shows the bounds on n_s in each of these cases.

These results slightly improve over the constraint $r_{0.002} < 0.12$ (95% CL) derived from the *Planck* 2013 temperature data in combination with WMAP large-scale polarization data (Planck Collaboration XVI 2014; Planck Collaboration XXII 2014). The constraint obtained by *Planck* temperature and polarization on large scales is tighter than the *Planck* B-mode 95% CL upper limit from the 100 and 143 GHz HFI channels, $r < 0.27$ (Planck Collaboration XI 2016). The constraints on r reported in Table 4 can be translated into upper bounds on the energy scale of inflation at the time when the pivot scale exits the Hubble radius using

$$V_* = \frac{3\pi^2 A_s}{2}\, r\, M_{\rm pl}^4 = (1.88 \times 10^{16}\ \mathrm{GeV})^4 \frac{r}{0.10}. \quad (26)$$

This gives an upper bound on the Hubble parameter during inflation of $H_*/M_{\rm pl} < 3.6 \times 10^{-5}$ (95% CL) for *Planck* TT+lowP.

These bounds are relaxed when allowing for a scale dependence of the scalar and tensor spectral indices. In that case, we assume that the tensor spectral index and its running are fixed by the standard inflationary consistency condition at second order in slow roll. We obtain

$$r_{0.002} < 0.18 \quad (95\%\ \mathrm{CL}, \textit{Planck}\ \mathrm{TT+lowP}), \quad (27)$$
$$\frac{\mathrm{d}n_s}{\mathrm{dln}\,k} = -0.013^{+0.010}_{-0.009} \quad (68\%\ \mathrm{CL}, \textit{Planck}\ \mathrm{TT+lowP}), \quad (28)$$

with $n_s = 0.9667 \pm 0.0066$ (68% CL). At the standard pivot scale, $k_* = 0.05\,\mathrm{Mpc}^{-1}$, the bound is stronger ($r < 0.17$ at 95% CL), because k_* is closer to the scale at which n_s and r decorrelate. The constraint on $r_{0.002}$ in Eq. (27) is 21% tighter than the corresponding *Planck* 2013 constraint. The mean value of the running in Eq. (28) is higher (lower in absolute value) than with *Planck* 2013 by 45%. Figures 5 and 6 clearly illustrate this significant improvement with respect to the previous *Planck* data release. Table 4 shows how bounds on (r, n_s, dn_s/dln k) are affected by

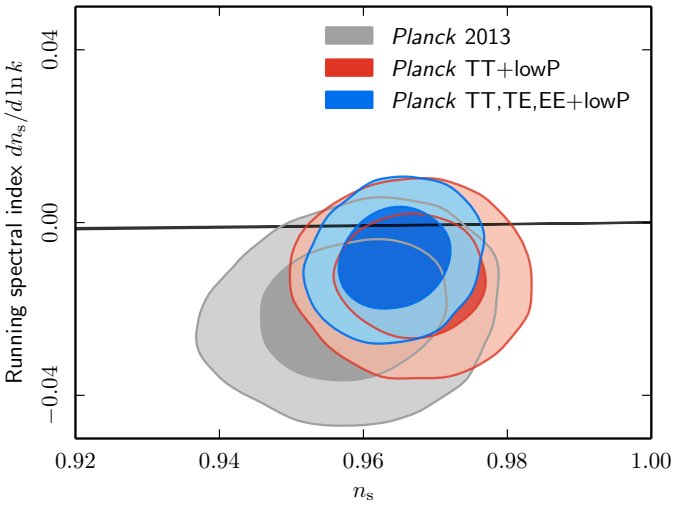

Fig. 5. Marginalized joint confidence contours for $(n_s, dn_s/d\ln k)$, at the 68% and 95% CL, in the presence of a non-zero tensor contribution, and using *Planck* TT+lowP or *Planck* TT, TE, EE+lowP. Constraints from the *Planck* 2013 data release are also shown for comparison. The thin black stripe shows the prediction of single-field monomial inflation models with $50 < N_* < 60$.

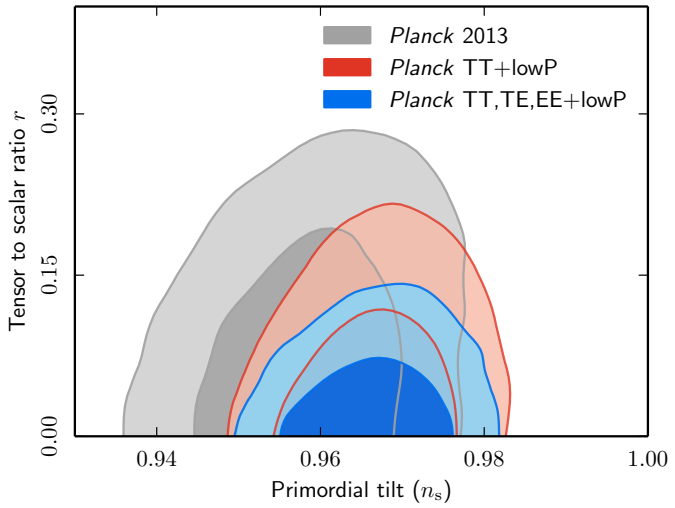

Fig. 6. Marginalized joint confidence contours for (n_s, r), at the 68% and 95% CL, in the presence of running of the spectral indices, and for the same data combinations as in the previous figure.

the lensing reconstruction, BAO, or high-ℓ polarization data. The tightest bounds are obtained in combination with polarization:

$$r_{0.002} < 0.15 \quad (95\%\ \text{CL}, \textit{Planck}\ \text{TT, TE, EE+lowP}), \tag{29}$$

$$\frac{dn_s}{d\ln k} = -0.009 \pm 0.008 \quad (68\%\ \text{CL}, \textit{Planck}\ \text{TT, TE, EE+lowP}), \tag{30}$$

with $n_s = 0.9644 \pm 0.0049$ (68% CL).

Neither the *Planck* full mission constraints in Eqs. (22)–(25) nor those including a running in Eqs. (27) and (29) are compatible with the interpretation of the BICEP2 *B*-mode polarization data in terms of primordial gravitational waves (BICEP2 Collaboration 2014b). Instead they are in excellent agreement with the results of the BICEP2/Keck Array-*Planck* cross-correlation analysis, as discussed in Sect. 13.

5.2. Dependence of the r constraints on the low-ℓ likelihood

The constraints on r discussed above are further tightened by adding WMAP polarization information on large angular scales. The *Planck* measurement of CMB polarization on large angular scales at 70 GHz is consistent with the WMAP 9-year one, based on the *K*, *Q*, and *V*-bands (at 30, 40, and 60 GHz, respectively), once the *Planck* 353 GHz channel is used to remove the dust contamination, instead of the theoretical dust model used by the WMAP team (Page et al. 2007). (For a detailed discussion, see Planck Collaboration XI 2016.) By combining *Planck* TT data with LFI 70 GHz and WMAP polarization data on large angular scales, we obtain a 35% reduction of uncertainty, giving $\tau = 0.074 \pm 0.012$ (68% CL) and $n_s = 0.9660 \pm 0.060$ (68% CL) for the base ΛCDM model. When tensors are added, the bounds become

$$r_{0.002} < 0.09 \quad (95\%\ \text{CL}, \textit{Planck}\ \text{TT+lowP+WP}), \tag{31}$$

$$n_s = 0.9655 \pm 0.058 \quad (68\%\ \text{CL}, \textit{Planck}\ \text{TT+lowP+WP}), \tag{32}$$

$$\tau = 0.073^{+0.011}_{-0.013} \quad (68\%\ \text{CL}, \textit{Planck}\ \text{TT+lowP+WP}). \tag{33}$$

When tensors and running are both varied, we obtain $r_{0.002} < 0.14$ (95% CL) and $dn_s/d\ln k = -0.010 \pm 0.008$ (68% CL) for *Planck* TT+lowP+WP. These constraints are all tighter than those based on *Planck* TT+lowP only.

5.3. The tensor-to-scalar ratio and the low-ℓ deficit in temperature

As noted previously (Planck Collaboration XV 2014; Planck Collaboration XVI 2014; Planck Collaboration XXII 2014), the low-ℓ temperature data display a slight lack of power compared to the expectation of the best-fit tensor-free base ΛCDM model. Since tensor fluctuations add power on small scales, the effect will be exacerbated in models allowing $r > 0$.

In order to quantify this tension, we compare the observed constraint on r to that inferred from simulated *Planck* data. In the simulations, we assume the underlying fiducial model to be tensor-free, with parameters close to the base ΛCDM best-fit values. We limit the simulations to mock temperature power spectra only and fit these spectra with an exact low-ℓ likelihood for $2 \le \ell \le 29$ (see Perotto et al. 2006), and a high-ℓ Gaussian likelihood for $30 \le \ell \le 2508$ based on the frequency-combined, foreground-marginalized, unbinned *Planck* temperature power spectrum covariance matrix. Additionally, we impose a Gaussian prior of $\tau = 0.07 \pm 0.02$.

Based on 100 simulated data sets, we find a 95% CL upper limit on the tensor-to-scalar ratio of $\bar{r}_{2\sigma} \approx 0.260$. The corresponding constraint from real data (using low-ℓ `Commander` temperature data, the frequency-combined, foreground-marginalized, unbinned *Planck* high-ℓ TT power spectrum, and the same prior on τ as above) reads $r < 0.123$, confirming that the actual constraint is tighter than what one would have expected. However, the actual constraint is not excessively unusual: out of the 100 simulations, 4 lead to an even tighter bound, corresponding to a significance of about 2σ. Thus, under the hypothesis of the base ΛCDM cosmology, the upper limit on r that we get from the data is not implausible as a chance fluctuation of the low multipole power.

To illustrate the contribution of the low-ℓ temperature power deficit to the estimates of cosmological parameters, we show as an example in Fig. 7 how n_s shifts towards lower values when the $\ell < 30$ temperature information is discarded (we will refer to this case as "*Planck* TT−lowT"). The shift in n_s is approximately

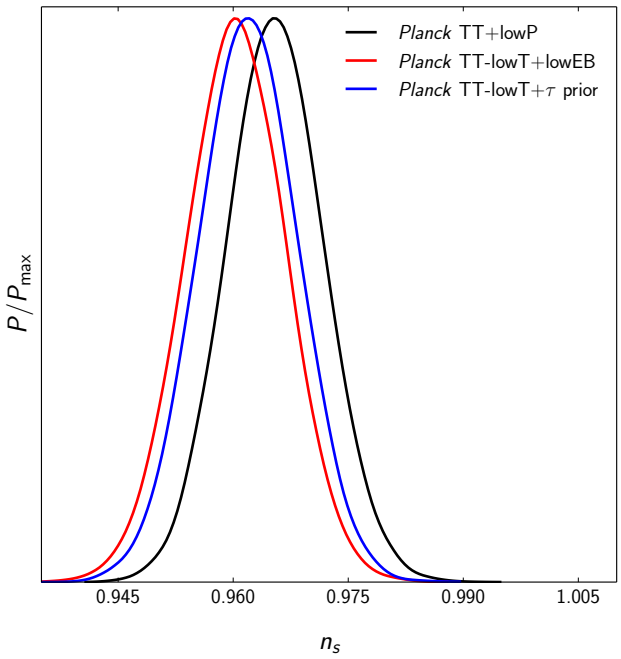

Fig. 7. One-dimensional posterior probabilities for n_s for the base ΛCDM model obtained by excluding temperature multipoles for $\ell < 30$ ("TT−lowT"), while either keeping low-ℓ polarization data, or in addition replacing them with a Gaussian prior on τ.

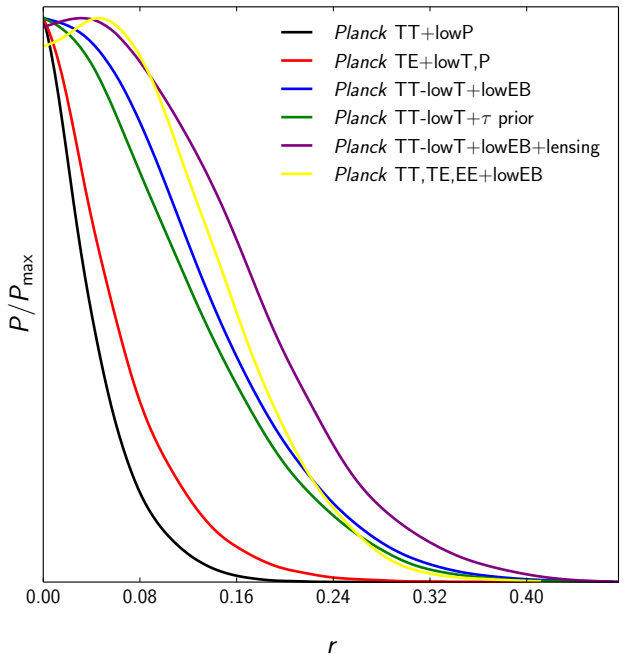

Fig. 8. One-dimensional posterior probabilities for r for various data combinations, either including or not including temperature multipoles for $\ell < 30$, and compared with the baseline choice (*Planck* TT+lowP, black curve).

-0.005 (or -0.003 when the lowP likelihood is replaced by a Gaussian prior $\tau = 0.07 \pm 0.02$). These shifts exceed those found in Sect. 4.4, where a primordial power spectrum suppressed on large scales was fitted to the data.

Figure 8 displays the posterior probability for r for various combinations of data sets, some of which exclude the $\ell < 30$ *TT* data. This leads to the very conservative bounds $r \lesssim 0.24$ and $r \lesssim 0.23$ at 95% CL when combined with the lowP likelihood or with the Gaussian prior $\tau = 0.07 \pm 0.020$, respectively.

5.4. Relaxing assumptions on the late-time cosmological evolution

As in the *Planck* 2013 release (PCI13), we now ask how robust the *Planck* results on the tensor-to-scalar ratio are against assumptions on the late-time cosmological evolution. The results are summarized in Table 5, and some particular cases are illustrated in Fig. 9. Constraints on r turn out to be remarkably stable for one-parameter extensions of the ΛCDM+r model, with the only exception the ΛCDM+r+Ω_K case in the absence of the late time information from *Planck* lensing or BAO data. The weak trend towards $\Omega_K < 0$, i.e., towards a positively curved (closed) universe from the temperature and polarization data alone, and the well-known degeneracy between Ω_K and $H_0/\Omega_{\rm m}$ lead to a slight suppression of the Sachs-Wolfe plateau in the scalar temperature spectrum. This leaves more room for a tensor component.

This further degeneracy when r is added builds on the negative values for the curvature allowed by *Planck* TT+lowP, $\Omega_K = -0.052^{+0.049}_{-0.055}$ at 95% CL (Planck Collaboration XIII 2016). The exploitation of the information contained in the *Planck* lensing likelihood leads to a tighter constraint, $\Omega_K = -0.005^{+0.016}_{-0.017}$ at 95% CL, which improves on the *Planck* 2013 results ($\Omega_K = -0.007^{+0.018}_{-0.019}$ at 95% CL). However, due to the remaining degeneracies left by the uncertainties in polarization on large angular scales, a full appreciation of the improvement due to the full mission temperature and lensing data can be obtained by using lowP+WP, which leads to $\Omega_K = -0.003^{+0.012}_{-0.014}$ at 95% CL. Note that the negative values allowed for the curvature are decreased in magnitude when the running is allowed, suggesting that the low-ℓ temperature deficit is contributing to the estimate of the spatial curvature.

The trend found for ΛCDM+r+Ω_K is even clearer when spatial curvature and the running of the spectral index are varied at the same time. In this case, the *Planck* temperature plus polarization data are compatible with r values as large as 0.19 (95% CL), at the cost of an almost 4σ deviation from spatial flatness (which, however, disappears as soon as lensing or BAO data are considered).

6. Implications for single-field slow-roll inflation

In this section we study the implications of *Planck* 2015 constraints on standard slow-roll single-field inflationary models.

6.1. Constraints on slow-roll parameters

We first present the *Planck* 2015 constraints on slow-roll parameters obtained through the analytic perturbative expansion in terms of the HFFs ϵ_i for the primordial spectra of cosmological fluctuations during slow-roll inflation (Stewart & Lyth 1993; Gong & Stewart 2001; Leach et al. 2002). When restricting to first order in ϵ_i, we obtain

$$\epsilon_1 < 0.0068 \qquad (95\%\ \text{CL}, \textit{Planck}\ \text{TT+lowP}), \tag{34}$$

$$\epsilon_2 = 0.029^{+0.008}_{-0.007} \qquad (68\%\ \text{CL}, \textit{Planck}\ \text{TT+lowP}). \tag{35}$$

When high-ℓ polarization is included we obtain $\epsilon_1 < 0.0066$ at 95% CL and $\epsilon_2 = 0.030^{+0.007}_{-0.006}$ at 68% CL. When second-order

Table 5. Constraints on extensions of the ΛCDM+r cosmological model for *Planck* TT+lowP+lensing, *Planck* TT+lowP+BAO, and *Planck* TT, TE, EE+lowP.

Extended model, ΛCDM+r+	Parameter	*Planck* TT+lowP +lensing	*Planck* TT+lowP +BAO	*Planck* TT, TE, EE +lowP
+general reionization	r	< 0.11	< 0.10	< 0.10
	n_s	0.975 ± 0.006	0.971 ± 0.005	0.968 ± 0.005
$+N_{\rm eff}$	r	< 0.14	< 0.12	< 0.11
	n_s	$0.977^{+0.016}_{-0.017}$	0.972 ± 0.009	0.964 ± 0.010
	$N_{\rm eff}$	$3.24^{+0.30}_{-0.35}$	3.19 ± 0.24	$3.02^{+0.20}_{-0.21}$
$+Y_{\rm He}$	r	< 0.14	< 0.12	< 0.12
	n_s	0.975 ± 0.007	0.973 ± 0.009	0.969 ± 0.008
	$Y_{\rm He}$	0.258 ± 0.022	0.257 ± 0.022	0.252 ± 0.014
$+\sum m_\nu$	r	< 0.11	< 0.11	< 0.11
	n_s	0.963 ± 0.007	0.967 ± 0.005	0.962 ± 0.005
	$\sum m_\nu$ [eV]	< 0.67	< 0.21	< 0.58
$+\Omega_K$	r	< 0.15	< 0.11	< 0.15
	n_s	0.971 ± 0.007	0.971 ± 0.007	0.969 ± 0.005
	Ω_K	$-0.008^{+0.010}_{-0.008}$	-0.001 ± 0.003	$-0.045^{+0.016}_{-0.020}$
$+w$	r	< 0.14	< 0.11	< 0.12
	n_s	0.969 ± 0.006	0.967 ± 0.006	0.966 ± 0.005
	w	$-1.46^{+0.20}_{-0.40}$	$-1.02^{+0.08}_{-0.07}$	$-1.57^{+0.17}_{-0.37}$
$+\Omega_K+{\rm d}n_s/{\rm d}\ln k$	r	< 0.20	< 0.18	< 0.19
	n_s	0.971 ± 0.007	0.969 ± 0.007	0.969 ± 0.005
	${\rm d}n_s/{\rm d}\ln k$	-0.006 ± 0.009	-0.013 ± 0.009	-0.004 ± 0.008
	Ω_K	$-0.006^{+0.010}_{-0.009}$	-0.001 ± 0.003	$-0.043^{+0.011}_{-0.020}$
$+N_{\rm eff}+m^{\rm eff}_{\nu,{\rm sterile}}$	r	< 0.14	< 0.13	< 0.12
	n_s	$0.980^{+0.010}_{-0.014}$	$0.978^{+0.008}_{-0.011}$	$0.968^{+0.006}_{-0.008}$
	$m^{\rm eff}_{\nu,{\rm sterile}}$ [eV]	< 0.59	< 0.55	< 0.83
	$N_{\rm eff}$	< 3.80	< 3.73	< 3.47

Notes. For each model we quote 68% CL, unless 95% CL upper bounds are reported.

contributions in the HFFs are included, we obtain

$$\epsilon_1 < 0.012 \qquad (95\%\ {\rm CL},\ \textit{Planck}\ {\rm TT+lowP}), \tag{36}$$

$$\epsilon_2 = 0.031^{+0.013}_{-0.011} \quad (68\%\ {\rm CL},\ \textit{Planck}\ {\rm TT+lowP}), \tag{37}$$

$$-0.41 < \epsilon_3 < 1.38 \qquad (95\%\ {\rm CL},\ \textit{Planck}\ {\rm TT+lowP}). \tag{38}$$

When high-ℓ polarization is included we obtain $\epsilon_1 < 0.011$ at 95% CL, $\epsilon_2 = 0.032^{+0.011}_{-0.009}$ at 68% CL, and $-0.32 < \epsilon_3 < 0.89$ at 95% CL.

The potential slow-roll parameters are obtained as derived parameters by using their exact expressions as function of ϵ_i (Leach et al. 2002; Finelli et al. 2010):

$$\epsilon_V = \frac{V_\phi^2 M_{\rm pl}^2}{2V^2} = \epsilon_1 \frac{\left(1 - \frac{\epsilon_1}{3} + \frac{\epsilon_2}{6}\right)^2}{\left(1 - \frac{\epsilon_1}{3}\right)^2}, \tag{39}$$

$$\eta_V = \frac{V_{\phi\phi} M_{\rm pl}^2}{V} = \frac{2\epsilon_1 - \frac{\epsilon_2}{2} - \frac{2\epsilon_1^2}{3} + \frac{5\epsilon_1\epsilon_2}{6} - \frac{\epsilon_2^2}{12} - \frac{\epsilon_2\epsilon_3}{6}}{1 - \frac{\epsilon_1}{3}}, \tag{40}$$

$$\xi_V^2 = \frac{V_{\phi\phi\phi} V_\phi M_{\rm pl}^4}{V^2} = \frac{1 - \frac{\epsilon_1}{3} + \frac{\epsilon_2}{6}}{\left(1 - \frac{\epsilon_1}{3}\right)^2} \left(4\epsilon_1^2 - 3\epsilon_1\epsilon_2 + \frac{\epsilon_2\epsilon_3}{2} - \epsilon_1\epsilon_2^2 + 3\epsilon_1^2\epsilon_2 - \frac{4}{3}\epsilon_1^3 - \frac{7}{6}\epsilon_1\epsilon_2\epsilon_3 + \frac{\epsilon_2^2\epsilon_3}{6} + \frac{\epsilon_2\epsilon_3^2}{6} + \frac{\epsilon_2\epsilon_3\epsilon_4}{6}\right), \tag{41}$$

where $V(\phi)$ is the inflaton potential, the subscript ϕ denotes the derivative with respect to ϕ, and $M_{\rm pl} = (8\pi G)^{-1/2}$ is the reduced Planck mass (see also Table 2).

By using Eqs. (39) and (40) with $\epsilon_3 = 0$ and the primordial power spectra to lowest order in the HFFs, the derived constraints for the first two slow-roll potential parameters are:

$$\epsilon_V < 0.0068 \qquad (95\%\ {\rm CL},\ \textit{Planck}\ {\rm TT+lowP}), \tag{42}$$

$$\eta_V = -0.010^{+0.005}_{-0.009} \qquad (68\%\ {\rm CL},\ \textit{Planck}\ {\rm TT+lowP}). \tag{43}$$

When high-ℓ polarization is included we obtain $\epsilon_V < 0.0067$ at 95% CL and $\eta_V = -0.010^{+0.004}_{-0.009}$ at 68% CL. By using Eqs. (39)–(41) with $\epsilon_4 = 0$ and the primordial power spectra to second order in the HFFs, the derived constraints for the slow-roll potential parameters are:

$$\epsilon_V < 0.012 \qquad (95\%\ {\rm CL},\ \textit{Planck}\ {\rm TT+lowP}), \tag{44}$$

$$\eta_V = -0.0080^{+0.0088}_{-0.0146} \qquad (68\%\ {\rm CL},\ \textit{Planck}\ {\rm TT+lowP}), \tag{45}$$

$$\xi_V^2 = 0.0070^{+0.0045}_{-0.0069} \qquad (68\,\%\ {\rm CL},\ \textit{Planck}\ {\rm TT+lowP}). \tag{46}$$

When high-ℓ polarization is included we obtain $\epsilon_V < 0.011$ at 95% CL, and $\eta_V = -0.0092^{+0.0074}_{-0.0127}$ and $\xi_V^2 = 0.0044^{+0.0037}_{-0.0050}$, both at 68% CL.

In Figs. 10 and 11 we show the 68% CL and 95% CL of the HFFs and the derived potential slow-roll parameters with and without the high-ℓ polarization and compare these values with the *Planck* 2013 results.

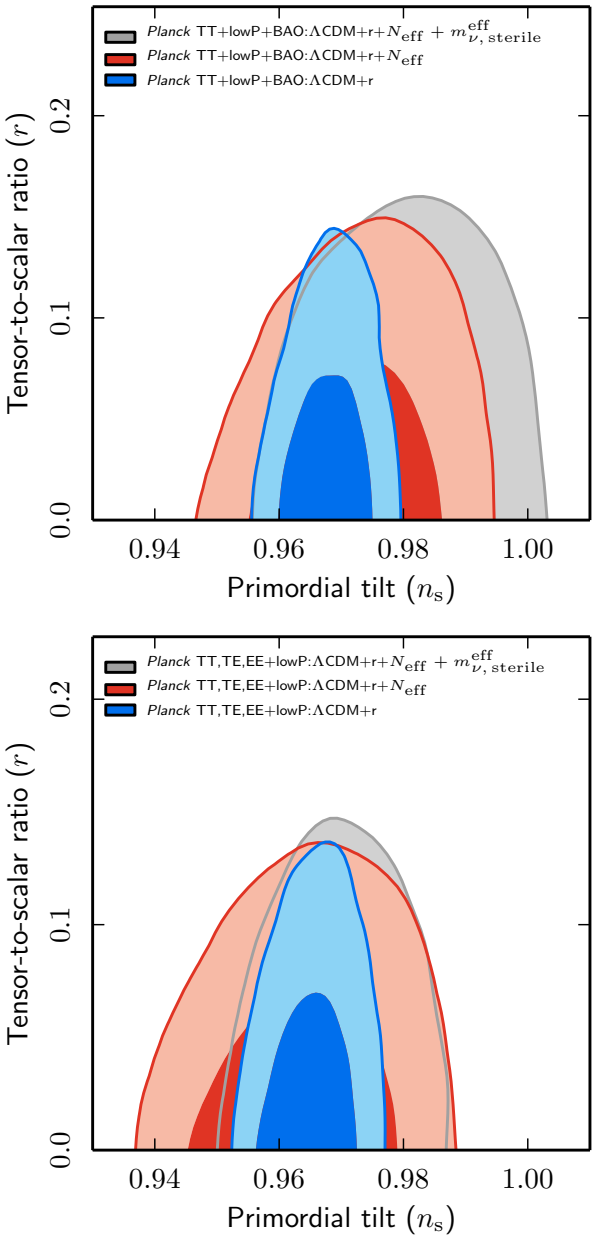

Fig. 9. Marginalized joint 68% and 95% CL for $(n_{\rm s}, r_{0.002})$ using *Planck* TT+lowP+BAO (*upper panel*) and *Planck* TT, TE, EE+lowP (*lower panel*).

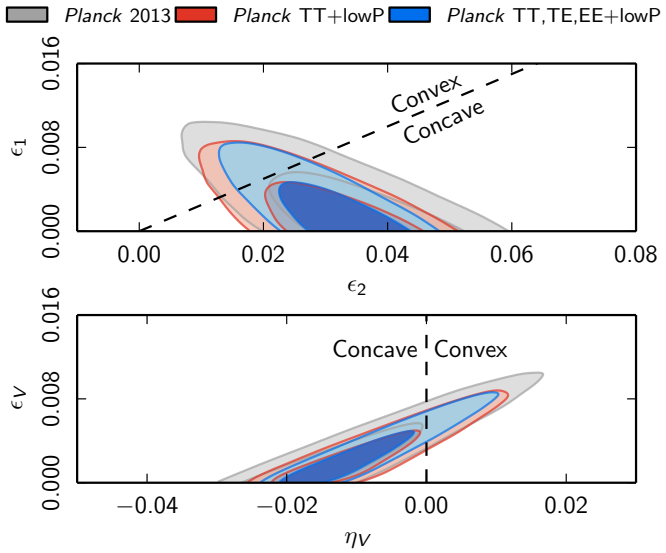

Fig. 10. Marginalized joint 68% and 95% CL regions for (ϵ_1, ϵ_2) (*top panel*) and (ϵ_V, η_V) (*bottom panel*) for *Planck* TT+lowP (red contours), *Planck* TT, TE, EE+lowP (blue contours), and compared with the *Planck* 2013 results (grey contours).

Table 6. Priors for cosmological parameters used in the Bayesian comparison of inflationary models.

Parameter range	Prior type
$0.019 < \Omega_{\rm b}h^2 < 0.025$	uniform
$0.095 < \Omega_{\rm c}h^2 < 0.145$	uniform
$1.03 < 100\theta_{\rm MC} < 1.05$	uniform
$0.01 < \tau < 0.4$	uniform

6.2. Implications for selected inflationary models

The predictions to lowest order in the slow-roll approximation for $(n_{\rm s}, r)$ at $k = 0.002\,{\rm Mpc}^{-1}$ of a few inflationary models with a representative uncertainty for the entropy generation stage ($50 < N_* < 60$) are shown in Fig. 12. Figure 12 updates Fig. 1 of PCI13 with the same notation.

In the following we discuss the implications of *Planck* TT+lowP+BAO data for selected slow-roll inflationary models by taking into account the uncertainties in the entropy generation stage. We model these uncertainties by two parameters, as in PCI13: the energy scale $\rho_{\rm th}$ by which the Universe has thermalized, and the parameter $w_{\rm int}$ which characterizes the effective equation of state between the end of inflation and the energy scale specified by $\rho_{\rm th}$. We use the primordial power spectra of cosmological fluctuations generated during slow-roll inflation parameterized by the HFFs, ϵ_i, to second order, which can be expressed in terms of the number of e-folds to the end of inflation, N_*, and the parameters of the considered inflationary model, using modified routines of the public code ASPIC[6] (Martin et al. 2014). For the number of e-folds to the end of inflation (Liddle & Leach 2003; Martin & Ringeval 2010) we use the expression (PCI13)

$$N_* \approx 67 - \ln\left(\frac{k_*}{a_0 H_0}\right) + \frac{1}{4}\ln\left(\frac{V_*^2}{M_{\rm pl}^4 \rho_{\rm end}}\right) + \frac{1-3w_{\rm int}}{12(1+w_{\rm int})}\ln\left(\frac{\rho_{\rm th}}{\rho_{\rm end}}\right) - \frac{1}{12}\ln(g_{\rm th}), \quad (47)$$

where $\rho_{\rm end}$ is the energy density at the end of inflation, $a_0 H_0$ is the present Hubble scale, V_* is the potential energy when k_* left the Hubble radius during inflation, $w_{\rm int}$ characterizes the effective equation of state between the end of inflation and the thermalization energy scale $\rho_{\rm th}$, and $g_{\rm th}$ is the number of effective bosonic degrees of freedom at the energy scale $\rho_{\rm th}$. We consider the pivot scale $k_* = 0.002\,{\rm Mpc}^{-1}$, $g_{\rm th} = 10^3$, and $\epsilon_{\rm end} = 1$. We consider the uniform priors for the cosmological parameters listed in Table 6. We also consider a logarithmic prior on $10^{10}A_{\rm s}$ (over the interval $[({\rm e}^{2.5}, {\rm e}^{3.7}])$ and $\rho_{\rm th}$ (over the interval $[(1\,{\rm TeV})^4, \rho_{\rm end}]$). We consider both the case in which $w_{\rm int}$ is kept fixed at zero and the case in which it is allowed to vary with a uniform prior in the range $-1/3 < w_{\rm int} < 1/3$.

[6] http://cp3.irmp.ucl.ac.be/~ringeval/aspic.html

Table 7. Results of the inflationary model comparison.

Inflationary model	$\Delta\chi^2$		$\ln B$	
	$w_{\rm int}=0$	$w_{\rm int}\neq 0$	$w_{\rm int}=0$	$w_{\rm int}\neq 0$
$R+R^2/(6M^2)$	+0.8	+0.3	...	+0.7
$n=2/3$	+6.5	+3.5	−2.4	−2.3
$n=1$	+6.2	+5.5	−2.1	−1.9
$n=4/3$	+6.4	+5.5	−2.6	−2.4
$n=2$	+8.6	+8.1	−4.7	−4.6
$n=3$	+22.8	+21.7	−11.6	−11.4
$n=4$	+43.3	+41.7	−23.3	−22.7
Natural	+7.2	+6.5	−2.4	−2.3
Hilltop ($p=2$)	+4.4	+3.9	−2.6	−2.4
Hilltop ($p=4$)	+3.7	+3.3	−2.8	−2.6
Double well	+5.5	+5.3	−3.1	−2.3
Brane inflation ($p=2$)	+3.0	+2.3	−0.7	−0.9
Brane inflation ($p=4$)	+2.8	+2.3	−0.4	−0.6
Exponential tails	+0.8	+0.3	−0.7	−0.9
SB SUSY	+0.7	+0.4	−2.2	−1.7
Supersymmetric α-model	+0.7	+0.1	−1.8	−2.0
Superconformal ($m=1$)	+0.9	+0.8	−2.3	−2.2
Superconformal ($m\neq 1$)	+0.7	+0.5	−2.4	−2.6

Notes. We provide $\Delta\chi^2$ with respect to base ΛCDM and Bayes factors with respect to R^2 inflation.

We have validated the slow-roll approach by cross-checking the Bayes factor computations against the fully numerical inflationary mode equation solver `ModeCode` coupled to the `PolyChord` sampler. For each inflationary model we provide in Table 7 and in the main text the $\Delta\chi^2$ value with respect to the base ΛCDM model, computed with the `CosmoMC` implementation of the BOBYQA algorithm for maximizing the likelihood, and the Bayesian evidence with respect to the R^2 inflationary model (Starobinsky 1980), computed by `CosmoMC` connected to `CAMB`, using `MultiNest` as the sampler.

Power law potentials

We first investigate the class of inflationary models with a single monomial potential (Linde 1983):

$$V(\phi)=\lambda M_{\rm pl}^4\left(\frac{\phi}{M_{\rm pl}}\right)^n, \tag{48}$$

in which inflation occurs for large values of the inflaton, $\phi > M_{\rm pl}$. The predictions for the scalar spectral index and the tensor-to-scalar ratio at first order in the slow-roll approximation are $n_{\rm s}-1\approx -2(n+2)/(4N_*+n)$ and $r\approx 16n/(4N_*+n)$, respectively. By assuming a dust equation of state (i.e., $w_{\rm int}=0$) prior to thermalization, the cubic and quartic potentials are strongly disfavoured by $\ln B=-11.6$ and $\ln B=-23.3$, respectively. The quadratic potential is moderately disfavoured by $\ln B=-4.7$. Other values, such as $n=4/3$, 1, and 2/3, motivated by axion monodromy (Silverstein & Westphal 2008; McAllister et al. 2010), are compatible with *Planck* data with $w_{\rm int}=0$.

Small modifications occur when considering the effective equation of state parameter, $w_{\rm int}=(n-2)/(n+2)$, defined by averaging over the coherent oscillation regime which follows inflation (Turner 1983). The Bayes factors are slightly modified when $w_{\rm int}$ is allowed to float, as shown in Table 7.

Hilltop models

In hilltop models (Boubekeur & Lyth 2005), with potential

$$V(\phi)\approx\Lambda^4\left(1-\frac{\phi^p}{\mu^p}+...\right), \tag{49}$$

the inflaton rolls away from an unstable equilibrium. The predictions to first order in the slow-roll approximation are $r\approx 8p^2(M_{\rm pl}/\mu)^2x^{2p-2}/(1-x^p)^2$ and $n_s-1\approx -2p(p-1)(M_{\rm pl}/\mu)^2x^{p-2}/(1-x^p)-3r/8$, where $x=\phi_*/\mu$. As in PCI13, the ellipsis in Eq. (49) and in what follows indicates higher-order terms that are negligible during inflation but ensure positiveness of the potential.

By sampling $\log_{10}(\mu/M_{\rm pl})$ within the prior $[0.30, 4.85]$ for $p=2$, we obtain $\log_{10}(\mu/M_{\rm pl})>1.02$ (1.05) at 95% CL and $\ln B=-2.6$ (−2.4) for $w_{\rm int}=0$ (allowing $w_{\rm int}$ to float).

An exact potential which could also apply after inflation, instead of the approximated one in Eq. (49), might be needed for a better comparison among different models. For $\mu/M_{\rm pl}\gg 1$, hilltop models as defined in Eq. (49) by neglecting the additional terms denoted by the ellipsis lead to $n_{\rm s}-1\approx -3r/8$, the same prediction as for the previously discussed linear potential, $V(\phi)\propto\phi$. By considering a double well potential, $V(\phi)=\Lambda^4[1-\phi^2/(2\mu^2)]^2$, instead, we obtain a slightly worse Bayes factor than the hilltop $p=2$ model, $\ln B=-3.1$ (−2.3) for $w_{\rm int}=0$ ($w_{\rm int}$ allowed to vary). This different result can be easily understood. Although the double well potential is equal to the hilltop model for $\phi\ll\mu$, it approximates $V(\phi)\propto\phi^2$ for $\mu/M_{\rm pl}\gg 1$. Since a linear potential is a better fit to *Planck* than ϕ^2, the fit of the double well potential is therefore worse than the hilltop $p=2$ case for $\mu/M_{\rm pl}\gg 1$, and this partially explains the slightly different Bayes factors obtained.

In the $p=4$ case, we obtain $\log_{10}(\mu/M_{\rm pl})>1.05$ (1.02) at 95% CL and $\ln B=-2.8$ (−2.6) for $w_{\rm int}=0$ (allowing $w_{\rm int}$ to float), assuming a prior range $[-2, 2]$ for $\log_{10}(\mu/M_{\rm pl})$.

Natural inflation

In *natural* inflation (Freese et al. 1990; Adams et al. 1993) a nonperturbative shift symmetry is invoked to suppress radiative corrections leading to the periodic potential

$$V(\phi)=\Lambda^4\left[1+\cos\left(\frac{\phi}{f}\right)\right], \tag{50}$$

where f is the scale which determines the curvature of the potential. We sample $\log_{10}(f/M_{\rm pl})$ within the prior $[0.3, 2.5]$ as in PCI13. We obtain $\log_{10}(f/M_{\rm pl})>0.84$ (>0.83) at 95% CL and $\ln B=-2.4$ (−2.3) for $w_{\rm int}=0$ (allowing $w_{\rm int}$ to vary).

Note that the super-Planckian value for f required by observations is not necessarily a problem for this class of models. When several fields ϕ_i with a cosine potential as in Eq. (50) and scales f_i appear in the Lagrangian, an effective single-field inflationary trajectory can be found for a suitable choice of parameters (Kim et al. 2005). In such a setting, the super-Planckian value of the effective scale f required by observations can be obtained even if the original scales satisfy $f_i\ll M_{\rm pl}$ (Kim et al. 2005).

D-brane inflation

Inflation can arise from physics involving extra dimensions. If the standard model of particle physics is confined to our

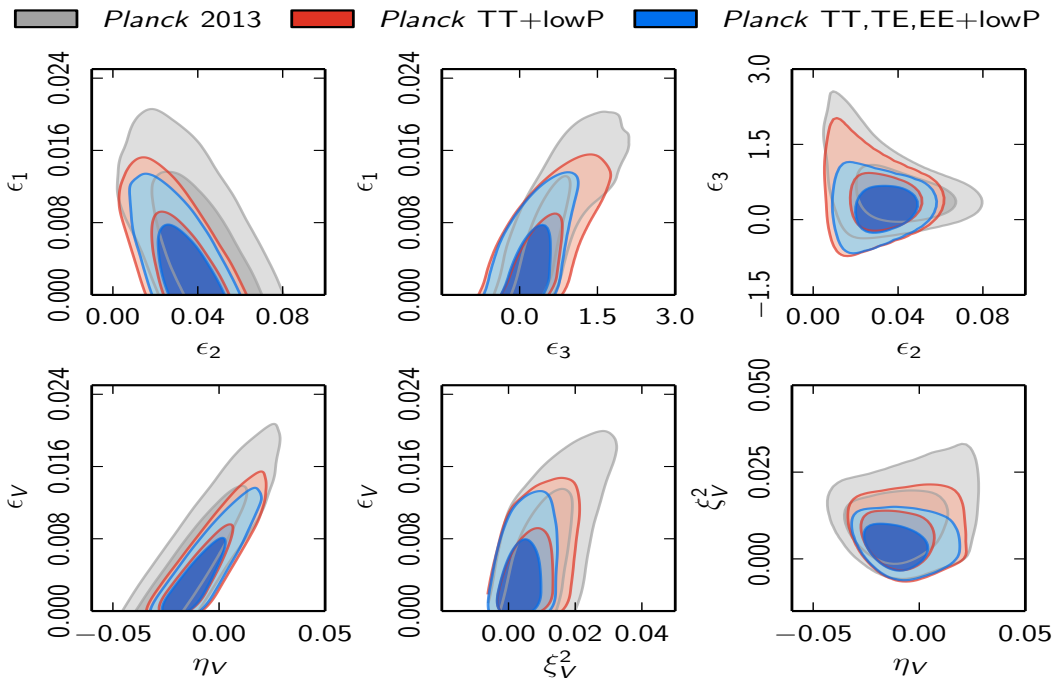

Fig. 11. Marginalized joint 68% and 95% CL regions for $(\epsilon_1, \epsilon_2, \epsilon_3)$ (*top panels*) and $(\epsilon_V, \eta_V, \xi_V^2)$ (*bottom panels*) for *Planck* TT+lowP (red contours), *Planck* TT, TE, EE+lowP (blue contours), and compared with the *Planck* 2013 results (grey contours).

3-dimensional brane, the distance between our brane and anti-brane can drive inflation. We consider the following parameterization for the effective potential driving inflation:

$$V(\phi) = \Lambda^4 \left(1 - \frac{\mu^p}{\phi^p} + ...\right). \tag{51}$$

Sampling $\log_{10}(\mu/M_{\rm pl})$ using a uniform prior over $[-6, 0.3]$, we consider $p = 4$ (Kachru et al. 2003; Dvali et al. 2001) and $p = 2$ (Garcia-Bellido et al. 2002). The predictions for r and $n_{\rm s}$ can be obtained from the hilltop case with the substitution $p \to -p$. These models agree with the *Planck* data with a Bayes factor of $\ln B = -0.4$ (-0.6) and $\ln B = -0.7$ (-0.9) for $p = 4$ and $p = 2$, respectively, for $w_{\rm int} = 0$ (allowing $w_{\rm int}$ to vary).

Potentials with exponential tails

Exponential potentials are ubiquitous in inflationary models motivated by supergravity and string theory (Goncharov & Linde 1984; Stewart 1995; Dvali & Tye 1999; Burgess et al. 2002; Cicoli et al. 2009). We restrict ourselves to analysing the following class of potentials:

$$V(\phi) = \Lambda^4 \left(1 - {\rm e}^{-q\phi/M_{\rm pl}} + ...\right). \tag{52}$$

As for the hilltop models described earlier, the ellipsis indicates possible higher-order terms that are negligible during inflation but ensure positiveness of the potential. These models predict $r \approx 8q^2{\rm e}^{-2q\phi/M_{\rm pl}}/(1 - {\rm e}^{-q\phi/M_{\rm pl}})^2$ and $n_s - 1 \approx -q^2{\rm e}^{-q\phi/M_{\rm pl}}(2 + {\rm e}^{-q\phi/M_{\rm pl}})/(1 - {\rm e}^{-q\phi/M_{\rm pl}})^2$ with a slow-roll trajectory characterized by $N \approx f(\phi/M_{\rm pl}) - f(\phi_{\rm end}/M_{\rm pl})$, with $f(x) = ({\rm e}^{qx} - qx)/q^2$. By sampling $\log_{10}(q/M_{\rm pl})$ with a uniform prior over $[-3, 3]$, we obtain a Bayes factor of -0.6 for $w_{\rm int} = 0$ $(-0.9$ when $w_{\rm int}$ is allowed to vary).

Spontaneously broken SUSY

Hybrid models (Copeland et al. 1994; Linde 1994) predicting $n_{\rm s} > 1$ are strongly disfavoured by the *Planck* data, as for the first cosmological release (PCI13). An example of a hybrid model predicting $n_{\rm s} < 1$ is the case in which slow-roll inflation is driven by loop corrections in spontaneously broken supersymmetric (SUSY) grand unified theories (Dvali et al. 1994) described by the potential

$$V(\phi) = \Lambda^4 \left[1 + \alpha_{\rm h} \log\left(\phi/M_{\rm pl}\right)\right], \tag{53}$$

where $\alpha_{\rm h} > 0$ is a dimensionless parameter. Note that for $\alpha_{\rm h} \ll 1$, this model leads to the same predictions as the power-law potential for $p \ll 1$ to lowest order in the slow-roll approximation. By sampling $\log_{10}(\alpha_{\rm h})$ on a flat prior $[-2.5, 1]$, we obtain a Bayes factor of -2.2 for $w_{\rm int} = 0$ $(-1.7$ when $w_{\rm int}$ is allowed to vary).

R^2 inflation

The first inflationary model proposed (Starobinsky 1980), with action

$$S = \int {\rm d}^4x\,\sqrt{-g}\frac{M_{\rm pl}^2}{2}\left(R + \frac{R^2}{6M^2}\right), \tag{54}$$

still lies within the *Planck* 68% CL constraints, as for the *Planck* 2013 release (PCI13). This model corresponds to the potential

$$V(\phi) = \Lambda^4 \left(1 - {\rm e}^{-\sqrt{2/3}\phi/M_{\rm pl}}\right)^2 \tag{55}$$

in the Einstein frame, which leads to the slow-roll predictions $n_{\rm s} - 1 \approx -2/N$ and $r \approx 12/N^2$ (Mukhanov & Chibisov 1981; Starobinsky 1983).

After the *Planck* 2013 release, several theoretical developments supported the model in Eq. (54) beyond the original motivation of including quantum effects at one-loop

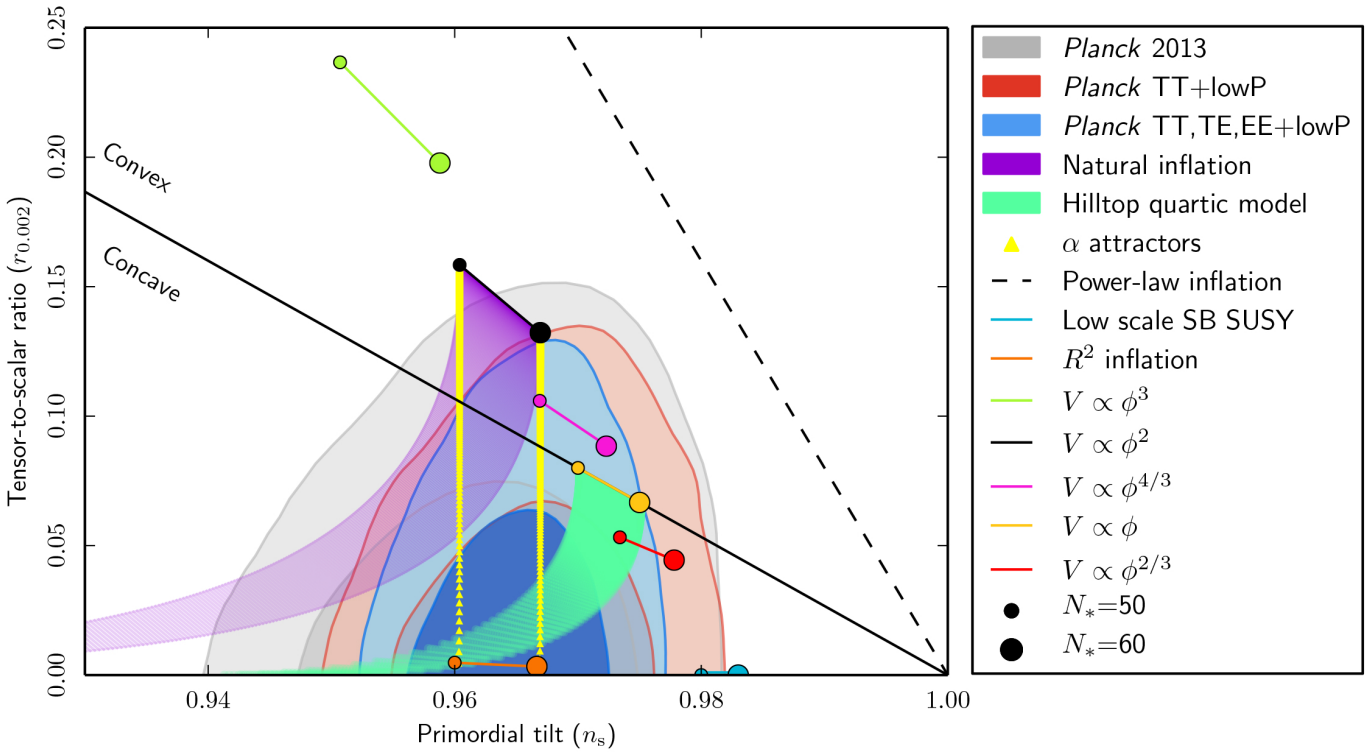

Fig. 12. Marginalized joint 68% and 95% CL regions for n_s and r at $k = 0.002\,\mathrm{Mpc}^{-1}$ from *Planck* compared to the theoretical predictions of selected inflationary models. Note that the marginalized joint 68% and 95% CL regions have been obtained by assuming $\mathrm{d}n_s/\mathrm{dln}\,k = 0$.

(Starobinsky 1980). No-scale supergravity (Ellis et al. 2013a), the large-field regime of superconformal D-term inflation (Buchmüller et al. 2013), or recent developments in minimal supergravity (Farakos et al. 2013; Ferrara et al. 2013b) can lead to a generalization of the potential in Eq. (55) (see Ketov & Starobinsky 2011 for a previous embedding of R^2 inflation in $F(\mathcal{R})$ supergravity). The potential in Eq. (55) can also be generated by spontaneous breaking of conformal symmetry (Kallosh & Linde 2013b). This inflationary model has $\Delta\chi^2 \approx 0.8$ (0.3) larger than the base ΛCDM model with no tensors for $w_{\rm int} = 0$ (for $w_{\rm int}$ allowed to vary). We obtain $54 < N_* < 62$ ($53 < N_* < 64$) at 95% CL for $w_{\rm int} = 0$ (for $w_{\rm int}$ allowed to vary), compatible with the theoretical prediction, $N_* = 54$ (Starobinsky 1980; Vilenkin 1985; Gorbunov & Panin 2011).

α attractors

We now study two classes of inflationary models motivated by recent developments in conformal symmetry and supergravity (Kallosh et al. 2013). The first class has been motivated by considering a vector rather than a chiral multiplet for the inflaton in supergravity (Ferrara et al. 2013a) and corresponds to the potential (Kallosh et al. 2013)

$$V(\phi) = \Lambda^4 \left(1 - \mathrm{e}^{-\sqrt{2}\phi/\left(\sqrt{3\alpha}M_{\rm pl}\right)}\right)^2. \tag{56}$$

To lowest order in the slow-roll approximation, these models predict $r \approx 64/[3\alpha(1 - \mathrm{e}^{\sqrt{2}\phi/(\sqrt{3\alpha}M_{\rm pl})})^2]$ and $n_s - 1 \approx -8(1 + \mathrm{e}^{\sqrt{2}\phi/(\sqrt{3\alpha}M_{\rm pl})})/[3\alpha(1 - \mathrm{e}^{\sqrt{2}\phi/(\sqrt{3\alpha}M_{\rm pl})})^2]$ based on an inflationary trajectory characterized by $N \approx g(\phi/M_{\rm pl}) - g(\phi_{\rm end}/M_{\rm pl})$ with $g(x) = (3\alpha^4 \mathrm{e}^{\sqrt{2}x/\sqrt{3\alpha}} - \sqrt{6\alpha}x)/4$. The relation between N and ϕ can be inverted through the use of the Lambert functions, as carried out for other potentials (Martin et al. 2014). By sampling $\log_{10}(\alpha^2)$ with a flat prior over $[0, 4]$, we obtain $\log_{10}(\alpha^2) < 1.7$ (2.0) at 95% CL and a Bayes factor of −1.8 (−2) for $w_{\rm int} = 0$ (for $w_{\rm int}$ allowed to vary).

The second class of models has been called super-conformal α attractors (Kallosh et al. 2013) and can be understood as originating from a different generating function with respect to the first class. This second class is described by the following potential (Kallosh et al. 2013):

$$V(\phi) = \Lambda^4 \tanh^{2m}\left(\frac{\phi}{\sqrt{6\alpha}M_{\rm pl}}\right). \tag{57}$$

This is the simplest class of models with spontaneous breaking of conformal symmetry, and for $\alpha = m = 1$ reduces to the original model introduced by Kallosh & Linde (2013b). The potential in Eq. (57) leads to the following slow-roll predictions (Kallosh et al. 2013):

$$r \approx \frac{48\alpha m}{4mN^2 + 2Ng(\alpha, m) + 3\alpha m}, \tag{58}$$

$$n_s - 1 \approx -\frac{8mN + 6\alpha m + 2g(\alpha, m)}{4mN^2 + 2Ng(\alpha, m) + 3\alpha m}, \tag{59}$$

where $g(\alpha, m) = \sqrt{3\alpha(4m^2 + 3\alpha)}$. The predictions of this second class of models interpolate between those of a large-field chaotic model, $V(\phi) \propto \phi^{2m}$, for $\alpha \gg 1$ and the R^2 model for $\alpha \ll 1$.

For α we adopt the same priors as for the previous class in Eq. (56). By fixing $m = 1$, we obtain $\log_{10}(\alpha^2) < 2.3$ (2.5) at 95% CL and a Bayes factor of −2.3 (−2.2) for $w_{\rm int} = 0$ (when $w_{\rm int}$ is allowed to vary). When m is allowed to vary as well with a flat prior in the range $[0, 2]$, we obtain $0.02 < m < 1$ ($m < 1$) at 95% CL for $w_{\rm int} = 0$ (when $w_{\rm int}$ is allowed to vary).

Non-minimally coupled inflaton

Inflationary predictions are quite sensitive to a non-minimal coupling $\xi R\phi^2$ of the inflaton to the Ricci scalar. One of the most interesting effects due to $\xi \neq 0$ is to reconcile the quartic potential $V(\phi) = \lambda\phi^4/4$ with *Planck* observations, even for $\xi \ll 1$. Non-minimal coupling leads as well to attractor behaviour towards predictions similar to those in R^2 inflation (Kaiser & Sfakianakis 2014; Kallosh & Linde 2013a).

The Higgs inflation model (Bezrukov & Shaposhnikov 2008), in which inflation occurs with $V(\phi) = \lambda(\phi^2 - \phi_0^2)^2/4$ and $\xi \gg 1$ for $\phi \gg \phi_0$, leads to the same predictions as the R^2 model to lowest order in the slow-roll approximation at tree level (see Barvinsky et al. 2008; and Bezrukov & Shaposhnikov 2009 for the inclusion of loop corrections). It is therefore in agreement with the *Planck* constraints, as for the first cosmological data release (PCI13).

We summarize below our findings for *Planck* lowP+BAO.

- Monomial potentials with integral $n > 2$ are strongly disfavoured with respect to R^2.
- The Bayes factor prefers R^2 over chaotic inflation with monomial quadratic potential by odds of 110:1 under the assumption of a dust equation of state during the entropy generation stage.
- R^2 inflation has the strongest evidence (i.e., the greatest Bayes factor) among the models considered here. However, care must be taken not to overinterpret small differences in likelihood lacking statistical significance.
- The models closest to R^2 in terms of evidence are brane inflation and exponential inflation, which have one more parameter than R^2. Both brane inflation considered in Eq. (51) and exponential inflation in Eq. (52) approximate the linear potential for a large portion of parameter space (for $\mu/M_{\rm pl} \gg 1$ and $q \gg 1$, respectively). For this reason these models have a higher Bayesian evidence (although not at a statistically significant level) than those that approximate a quadratic potential, as do α-attractors, for instance.
- In the models considered here, the $\Delta\chi^2$ obtained by allowing w to vary is modest (i.e., less than approximately 1.6 with respect to $w_{\rm int} = 0$). The gain in the logarithm of the Bayesian evidence is even smaller, since an extra parameter is added.

7. Reconstruction of the potential and analysis beyond slow-roll approximation

7.1. Introdution

In the previous section, we derived constraints on several types of inflationary potentials assumed to account for the inflaton dynamics between the time at which the largest observable scales crossed the Hubble radius during inflation and the end of inflation. The full shape of the potential was used in order to identify when inflation ends, and thus the field value ϕ_* when the pivot scale crosses the Hubble radius.

In Sect. 6 of PCI13, we explored another approach, consisting of reconstructing the inflationary potential within its observable range without making any assumptions concerning the inflationary dynamics outside that range. Indeed, given that the number of e-folds between the observable range and the end of inflation can always be adjusted to take a realistic value, any potential shape giving a primordial spectrum of scalar and tensor perturbations in agreement with observations is a valid candidate. Inflation can end abruptly by a phase transition, or can last a long time if the potential becomes very flat after the observable region has been crossed. Moreover, there could be a short inflationary stage responsible for the origin of observable cosmological perturbations, and another inflationary stage later on (but before nucleosynthesis), thus contributing to the total N_*.

In Sect. 6 of PCI13, we performed this analysis with a full integration of the inflaton and metric perturbation modes, so that no slow-roll approximation was made. The only assumption was that primordial scalar perturbations are generated by the fluctuations of a single inflaton field with a canonical kinetic term. Since in this approach one is only interested in the potential over a narrow range of observable scales (centred around the field value ϕ_* when the pivot scale crosses the Hubble radius), it is reasonable to test relatively simple potential shapes described by a small number of free parameters.

This approach gave very similar results to calculations based on the standard slow-roll analysis. This agreement can be explained by the fact that the *Planck* 2013 data already preferred a primordial spectrum very close to a power law, at least over most of the observable range. Hence the 2013 data excluded strong deviations from slow-roll inflation, which would either produce a large running of the spectral index or imprint more complicated features on the primordial spectrum. However, this conclusion did not apply to the largest scales observable by *Planck*, for which cosmic variance and slightly anomalous data points remained compatible with significant deviations from a simple power law spectrum. The most striking result in Sect. 6 of PCI13 was that a less restricted functional form for the inflaton potential gave results compatible with a rather steep potential at the beginning of the observable window, leading to a "not-so-slow" roll stage during the first few observable e-folds. This explains the shape of the potential in Fig. 14 of PCI13 for a Taylor expansion at order $n = 4$ and in the region where $\phi - \phi_* \leq -0.2$. However, such features were only partially explored because the method used for potential reconstruction did not allow for an arbitrary value of the inflation velocity $\dot\phi$ at the beginning of the observable window. Instead, our code imposed that the inflaton already tracked the inflationary attractor solution when the largest observable modes crossed the Hubble scale.

Given that the *Planck* 2015 data establish even stronger constraints on the primordial power spectrum than the 2013 results, it is of interest to revisit the reconstruction of the potential $V(\phi)$. Section 7.2 presents some new results following the same approach as in PCI13 (explained previously in Lesgourgues & Valkenburg 2007; and Mortonson et al. 2011). But in the present work, we also present some more general results, independent of any assumption concerning the initial field velocity $\dot\phi$ when the inflaton enters the observable window. Following previous studies (Kinney 2002; Kinney et al. 2006; Peiris & Easther 2006a,b, 2008; Easther & Peiris 2006; Lesgourgues et al. 2008; Powell & Kinney 2007; Hamann et al. 2008; Norena et al. 2012), we reconstruct the Hubble function $H(\phi)$, which determines both the potential $V(\phi)$ through

$$V(\phi) = 3M_{\rm Pl}^2 H^2(\phi) - 2M_{\rm Pl}^4 \left[H'(\phi)\right]^2, \tag{60}$$

and the solution $\phi(t)$ through

$$\dot\phi = -2M_{\rm Pl}^2 H'(\phi), \tag{61}$$

with $H'(\phi) = \partial H/\partial\phi$. Note that these two relations are exact. In Sect. 7.3, we fit $H(\phi)$ directly to the data, implicitly including all canonical single-field models in which the inflaton is rolling not very slowly (ϵ not much smaller than unity) just before entering the observable window, and the issue of having to start

Table 8. Numerical reconstruction of the potential slow-roll parameters *beyond* any slow-roll approximation when the potential is Taylor expanded to nth order, using *Planck* TT+lowP+BAO.

n	2	3	4
ϵ_V	<0.0074	<0.010	$0.0072^{+0.0093}_{-0.0069}$
η_V	$-0.007^{+0.014}_{-0.012}$	$-0.020^{+0.021}_{-0.018}$	$0.021^{+0.044}_{-0.042}$
ξ^2_V	...	$0.006^{+0.010}_{-0.010}$	$-0.018^{+0.028}_{-0.027}$
ϖ^3_V	...	...	$0.015^{+0.016}_{-0.017}$
τ	$0.083^{+0.036}_{-0.036}$	$0.096^{+0.046}_{-0.044}$	$0.102^{+0.046}_{-0.045}$
n_s	$0.9692^{+0.0094}_{-0.0093}$	$0.9689^{+0.0097}_{-0.0097}$	$0.964^{+0.011}_{-0.011}$
$dn_s/d\ln k$	$-0.00034^{+0.00055}_{-0.00059}$	$-0.013^{+0.019}_{-0.019}$	$0.003^{+0.026}_{-0.026}$
$r_{0.002}$	<0.11	<0.16	$0.11^{+0.16}_{-0.11}$
$\Delta\chi^2$	...	$\Delta\chi^2_{3/2} = -1.2$	$\Delta\chi^2_{4/3} = -2.1$
$\Delta\ln B$	...	$\Delta\ln B_{3/2} = -4.3$	$\Delta\ln B_{4/3} = -2.9$

Notes. We also show the corresponding bounds on the derived parameters (here n_s, $dn_s/d\ln k$, and $r_{0.002}$ are derived from the numerically computed primordial spectra). All error bars are at the 95% CL. The effective χ^2 value and Bayesian evidence logarithm ($\ln B$) of model n are given relative to the model of next lowest order ($n-1$) (assuming flat priors for ξ^2_V and ϖ^3_V in the range $[-1,1]$).

sufficiently early in order to allow the initial transient to decay is avoided. The only drawback in reconstructing $H(\phi)$ is that one cannot systematically test the simplest analytic forms for $V(\phi)$ in the observable range (for instance, polynomials of order $n = 1, 3, 5, \ldots$ in $(\phi - \phi_*)$). But our goal in this section is to explore how much one can deviate from slow-roll inflation in general, independently of the shape of the underlying inflaton potential.

7.2. Reconstruction of a smooth inflaton potential

Following the approach of PCI13, we Taylor expand the inflaton potential around $\phi = \phi_*$ to order $n = 2, 3, 4$. To obtain faster-converging Markov chains, instead of imposing flat priors on the Taylor coefficients $\{V, V_\phi, \ldots, V_{\phi\phi\phi\phi}\}$, we sample the potential slow-roll (PSR) parameters $\{\epsilon_V, \eta_V, \xi^2_V, \varpi^3_V\}$ related to the former as indicated in Table 2. We stress that this is just a choice of prior and does not imply any kind of slow-roll approximation in the calculation of the primordial spectra.

The results are given in Table 8 (for *Planck* TT+lowP+BAO) and Fig. 13 (for the same data set and also for *Planck* TT, TE, EE+lowP). The second part of Table 8 shows the corresponding values of the spectral parameters n_s, $dn_s/d\ln k$, and $r_{0.002}$ as measured for each numerical primordial spectrum (at the pivot scales $k = 0.05\,\mathrm{Mpc}^{-1}$ for the scalar and $0.002\,\mathrm{Mpc}^{-1}$ for the tensor spectra), as well as the reionization optical depth. We also show in Fig. 14 the derived distribution of each coefficient V_i (with a non-flat prior) and in Fig. 15 the reconstructed shape of the best-fit inflation potentials in the observable window. Finally, the posterior distribution of the derived parameters $r_{0.002}$ and $dn_s/d\ln k$ is displayed in Fig. 16.

Figure 13 shows that bounds are very similar when temperature data are combined with either high-ℓ polarization data or BAO data. This gives a hint of the robustness of these results. For

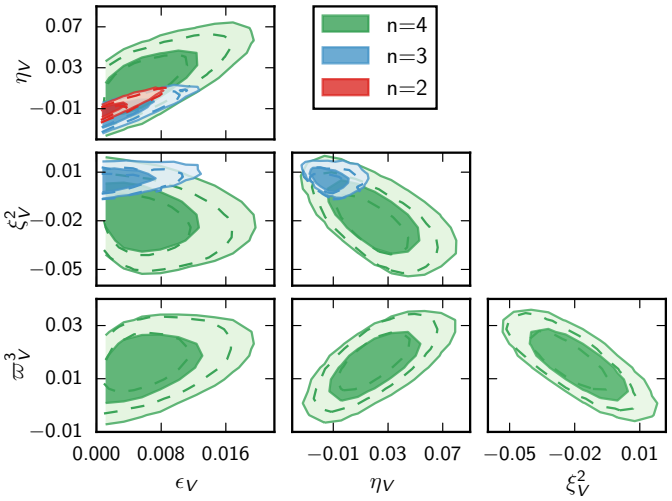

Fig. 13. Posterior distributions for the first four potential slow-roll parameters when the potential is Taylor expanded to nth order using *Planck* TT+lowP+BAO (filled contours) or TT, TE, EE+lowP (dashed contours). The primordial spectra are computed *beyond* the slow-roll approximation.

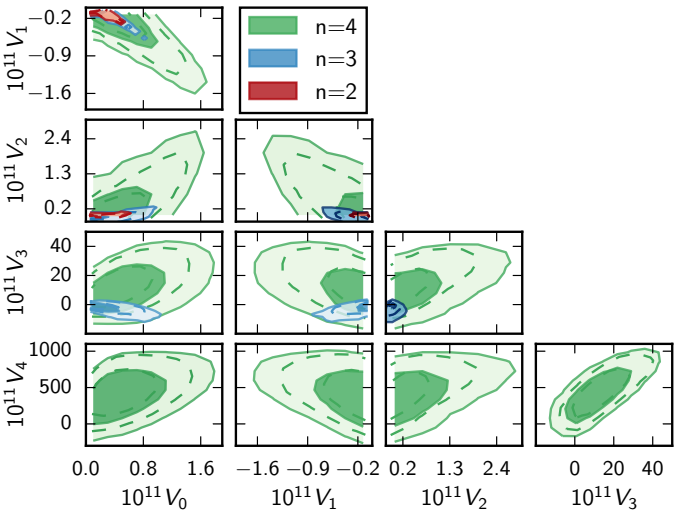

Fig. 14. Posterior distributions for the coefficients of the inflation potential Taylor expanded to nth order (in natural units where $\sqrt{8\pi}M_{\rm pl} = 1$) reconstructed *beyond* the slow-roll approximation using *Planck* TT+lowP+BAO (filled contours) or TT, TE, EE+lowP (dashed contours). The plot shows only half of the results; the other half is symmetric, with opposite signs for V_ϕ and $V_{\phi\phi\phi}$. Note that, unlike Fig. 13, the parameters shown here do *not* have flat priors, since they are mapped from the slow-roll parameters.

both data sets, the error bars on the PSR parameters are typically smaller by a factor of 1.5 than in PCI13.

Since potentials with $n = 2$ cannot generate a significant running, the bounds on the scalar spectral index and the tensor-to-scalar ratio and the best-fit models are very similar to those obtained with the ΛCDM+r model in Sect. 5 and Table 4. On the other hand, in the $n = 3$ model, results follow the trend of the previous ΛCDM+r+$dn_s/d\ln k$ analysis. The data prefer potentials with V_ϕ and $V_{\phi\phi\phi}$ of the same sign, generating a significant negative running (as can be seen in Fig. 16). This trend for $V_{\phi\phi\phi}$ occurs because a scalar spectrum with negative running reduces the power on large scales, and provides a better fit to

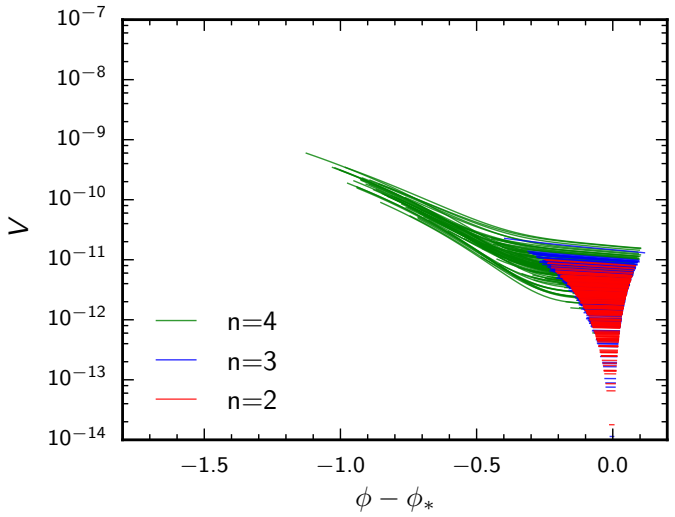

Fig. 15. Observable range of the best-fit inflaton potentials, when $V(\phi)$ is Taylor expanded to the nth order around the pivot value ϕ_* in natural units (where $\sqrt{8\pi}M_{\rm pl} = 1$) assuming a flat prior on ϵ_V, η_V, ξ_V^2, and ϖ_V^3 and using *Planck* TT+lowP+BAO. Potentials obtained under the transformation $(\phi - \phi_*) \to (\phi_* - \phi)$ leave the same observable signature and are also allowed. The sparsity of potentials with a small $V_0 = V(\phi_*)$ is due to our use of a flat prior on ϵ_V rather than on $\ln(V_0)$; in fact, V_0 is unbounded from below in the $n = 2$ and 3 results. The axis ranges are identical to those in Fig. 20, to make the comparison easier.

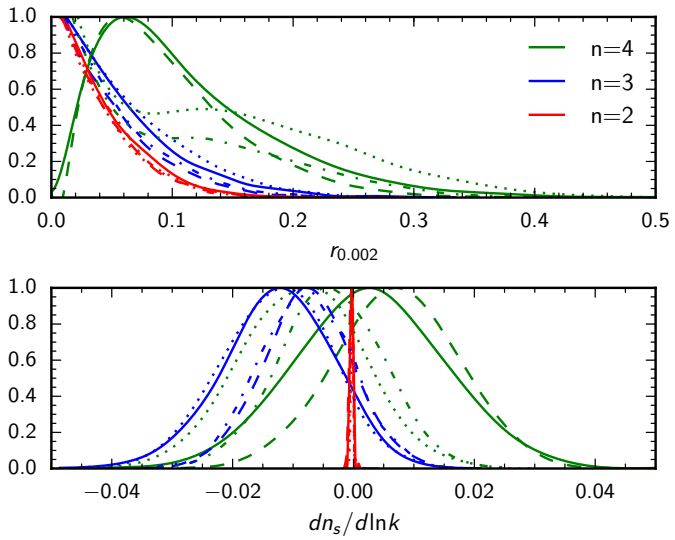

Fig. 16. Posterior distribution for the tensor-to-scalar ratio (at $k = 0.002\,\mathrm{Mpc}^{-1}$) and for the running parameter $\mathrm{d}n_s/\mathrm{d}\ln k$ (at $k = 0.05\,\mathrm{Mpc}^{-1}$), for the potential reconstructions in Sects. 7.2 and 7.3. The $V(\phi)$ reconstruction gives the solid curves for *Planck* TT+lowP+BAO, or dashed for TT, TE, EE+lowP. The $H(\phi)$ reconstruction gives the dotted curves for *Planck* TT+lowP+BAO, or dashed-dotted for TT, TE, EE+lowP. The tensor-to-scalar ratio appears as a derived parameter, but by taking a flat prior on either ϵ_V or $\epsilon_{\rm H}$, we implicitly also take a nearly flat prior on r. The same applies to $\mathrm{d}n_s/\mathrm{d}\ln k$.

low-ℓ temperature multipoles. However, such a running also suppresses power on small scales, so ξ_V^2 cannot be too large.

The $n = 4$ case possesses a new feature. The potential has more freedom to generate complicated shapes which would roughly correspond to a running of the running of the tilt (as studied in Sect. 4). The best-fit models now have V_ϕ and $V_{\phi\phi\phi}$ of opposite sign, and a large positive $V_{\phi\phi\phi\phi}$. The preferred

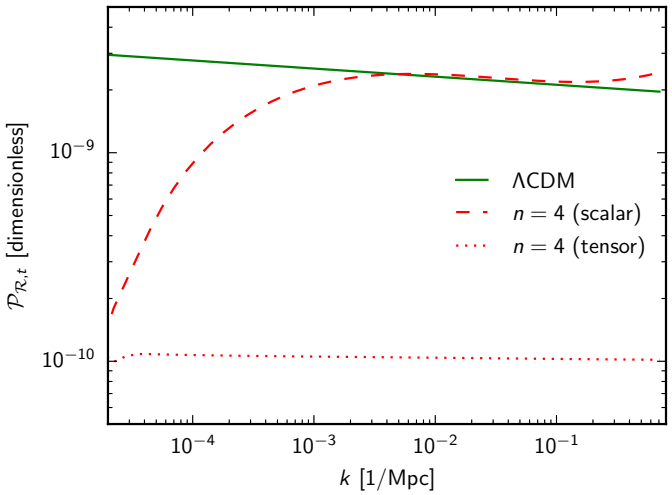

Fig. 17. Primordial spectra (scalar and tensor) of the best-fit $V(\phi)$ model with $n = 4$, for the *Planck* TT, TE, EE+lowP data set, compared to the primordial spectrum (scalar only) of the best-fit base ΛCDM model. The best-fit potential is initially very steep, as can be seen in Fig. 15 (note the typical shape of the green curves). The transition from "marginal slow roll" ($\epsilon_V(\phi)$ between 0.01 and 1) to "full slow roll" ($\epsilon_V(\phi)$ of order 0.01 or smaller) is responsible for the suppression of the large-scale scalar spectrum.

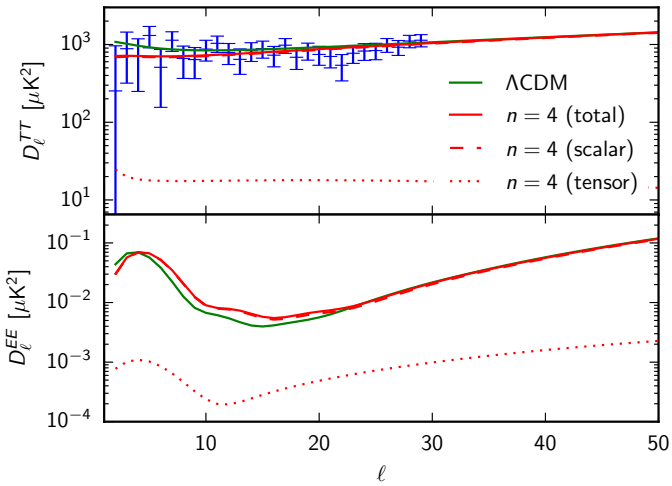

Fig. 18. Temperature and polarization spectra (total, scalar contribution, tensor contribution) of the best-fit $V(\phi)$ model with $n = 4$, for the *Planck* TT, TE, EE+lowP data set, compared to the spectra (scalar contribution only) of the best-fit base model. We also show the *Planck* low-ℓ temperature data, which is driving the small differences between the two best-fit models.

combination of these parameters allows for even more suppression of power on large scales, while leaving small scales nearly unchanged. This can be seen clearly from the shape of the scalar primordial spectrum corresponding to the best-fit models, for both data sets *Planck* TT+lowP+BAO and *Planck* TT, TE, EE+lowP. These two best-fit models are very similar, but in Fig. 17 we show the one for *Planck* TT, TE, EE+lowP, for which the trend is even more pronounced. Interestingly, the preferred models are such that power on large scales is suppressed in the scalar spectrum and balanced by a small tensor contribution, of roughly $r_{0.002} \sim 0.05$. This particular combination gives the best fit to the low-ℓ data, shown in Fig. 18, while leaving the high-ℓ temperature spectrum identical to the best fit base ΛCDM model.

Inflation produces such primordial perturbations with the family of green potentials displayed in Fig. 15. At the beginning of the observable range, the potential is very steep [$\epsilon_V(\phi)$ decreases from $O(1)$ to $O(10^{-2})$], and produces a low amplitude of curvature perturbations (allowing a rather large tensor contribution, up to $r_{0.002} \sim 0.3$). Then there is a transition towards a second region with a much smaller slope, leading to a nearly power-law curvature spectrum with the usual tilt value $n_s \approx 0.96$. In Fig. 15, one can check that the height of the $n = 4$ potentials varies in a definite range, while the $n = 2$ and 3 potentials can have arbitrarily small amplitude at the pivot scale, reflecting the posteriors on ϵ_V or r.

However, the improvement in χ^2 between the base ΛCDM and $n = 4$ models is only 2.2 (for *Planck* TT+lowP+BAO) or 4.3 (for *Planck* TT, TE, EE+lowP). This is marginal and offers no statistically significant evidence in favour of these complicated models. This conclusion is also supported by the calculation of the Bayesian evidence ratios, shown in the last line of Table 8 (under the assumption of flat priors in the range $[-1, 1]$ for ξ_V^2 and ϖ_V^3): the evidence decreases each time that a new free parameter is added to the potential. At the 95% CL, $r_{0.002}$ is still compatible with zero, and so are the higher order PSR parameters ξ_V^2 and ϖ_V^3. More freedom in the inflaton potential allows fitting the data better, but under the assumption of a smooth potential in the observable range, a simple quadratic form provides the best explanation of the *Planck* observations.

With the *Planck* TT+lowP+BAO and TT, TE, EE+lowP data sets, models with a large running or running of the running can be compatible with an unusually large value of the optical depth, as can be seen in Table 8. Including lensing information helps to break the degeneracy between the optical depth and the primordial amplitude of scalar perturbations. Hence the *Planck* lensing data could be used to strengthen the conclusions of this section.

Since in the $n = 4$ model, slow roll is marginally satisfied at the beginning of observable inflation, the reconstruction is very sensitive to the condition that there is an attractor solution at that time. Hence this case can in principle be investigated in a more conservative way using the $H(\phi)$ reconstruction method of the next section.

7.3. Reconstruction of a smooth Hubble function

In this section, we assume that the shape of the function $H(\phi)$ is well captured within the observable window by a polynomial of order n (corresponding to a polynomial inflaton potential of order $2n$):

$$H(\phi) = \sum_{i=0}^{n} H_i \frac{\phi^i}{i!}. \tag{62}$$

We vary n between 2 and 4. To avoid parameter degeneracies, as in the previous section we assume flat priors not on the Taylor coefficient H_i, but on the Hubble slow-roll (HSR) parameters, which are related according to

$$\epsilon_H = 2M_{pl}^2 \left(\frac{H_1}{H_0}\right)^2, \qquad \eta_H = 2M_{pl}^2 \frac{H_2}{H_0}, \tag{63}$$

$$\xi_H^2 = \left(2M_{pl}^2\right)^2 \frac{H_1 H_3}{H_0^2}, \qquad \varpi_H^3 = \left(2M_{pl}^2\right)^3 \frac{H_1^2 H_4}{H_0^3}. \tag{64}$$

This is just a choice of prior. This analysis does not rely on the slow-roll approximation.

Table 9 and Fig. 19 show our results for the reconstructed HSR parameters. Figure 20 shows a representative sample of potential shapes $V(\phi - \phi_*)$ derived using Eq. (60), for a sample of models drawn randomly from the chains, for the three cases $n = 2, 3, 4$.

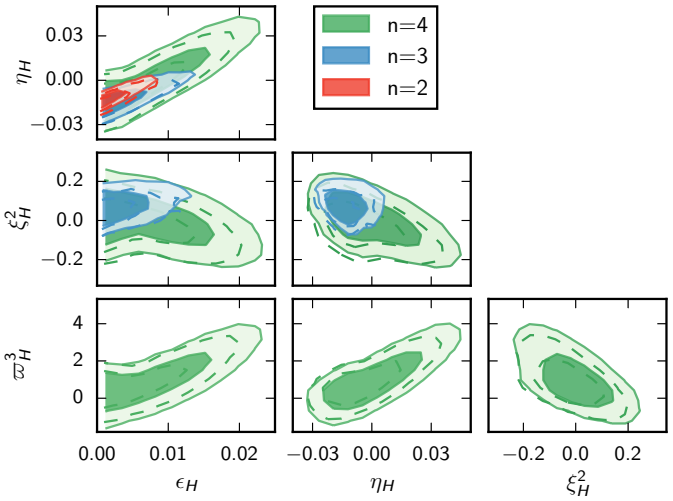

Fig. 19. Posterior distributions for the first four Hubble slow-roll parameters, when $H(\phi)$ is Taylor expanded to nth order, using *Planck* TT+lowP+BAO (filled contours) or TT, TE, EE+lowP (dashed contours). The primordial spectra are computed *beyond* the slow-roll approximation.

Table 9. Numerical reconstruction of the Hubble slow-roll parameters *beyond* the slow-roll approximation, using *Planck* TT+lowP+BAO.

n	2	3	4
ϵ_H	<0.0073	<0.011	<0.020
η_H	$-0.010^{+0.011}_{-0.009}$	$-0.012^{+0.015}_{-0.013}$	$-0.001^{+0.033}_{-0.027}$
ξ_H^2	...	$0.08^{+0.12}_{-0.12}$	$-0.01^{+0.19}_{-0.19}$
ϖ_H^3	...	...	$1.0^{+2.3}_{-1.8}$
τ	$0.082^{+0.038}_{-0.036}$	$0.096^{+0.042}_{-0.043}$	$0.096^{+0.042}_{-0.042}$
n_s	$0.9693^{+0.0094}_{-0.0093}$	$0.9680^{+0.0096}_{-0.0096}$	$0.967^{+0.010}_{-0.010}$
$10^3 \mathrm{d}n_s/\mathrm{d}\ln k$	$-0.251^{+0.41}_{-0.41}$	-13^{+18}_{-19}	-8^{+21}_{-21}
$r_{0.002}$	<0.11	<0.16	<0.32
$\Delta\chi^2$	...	$\Delta\chi^2_{3/2} = -0.6$	$\Delta\chi^2_{4/3} = -2.3$

Notes. We also show the corresponding bounds on some related parameters (here n_s, $\mathrm{d}n_s/\mathrm{d}\ln k$, and $r_{0.002}$ are derived from the numerically computed primordial spectra). All error bars are at the 95% CL. The effective χ^2 value of model n is given relative to model $n - 1$.

Most of the discussion of Sect. 7.2 also applies to this section, and so will not be repeated. Results for *Planck* TT+lowP+BAO and TT, TE, EE+lowP are still very similar. The $n = 2$ case still gives results close to ΛCDM+r, and the $n = 3$ case to ΛCDM+r+$\mathrm{d}n_s/\mathrm{d}\ln k$. The type of potential preferred in the $n = 4$ case is very similar to the $n = 4$ analysis of the previous section, for the reasons explained in Sect. 7.2. There are, however, small differences, because the range of parametric forms for the potential explored by the two analyses differ. In the $H(\phi)$ reconstruction, the underlying potentials $V(\phi)$ are not polynomials. In the first approximation, they are close to polynomials of order $2n$, but with constraints between the various

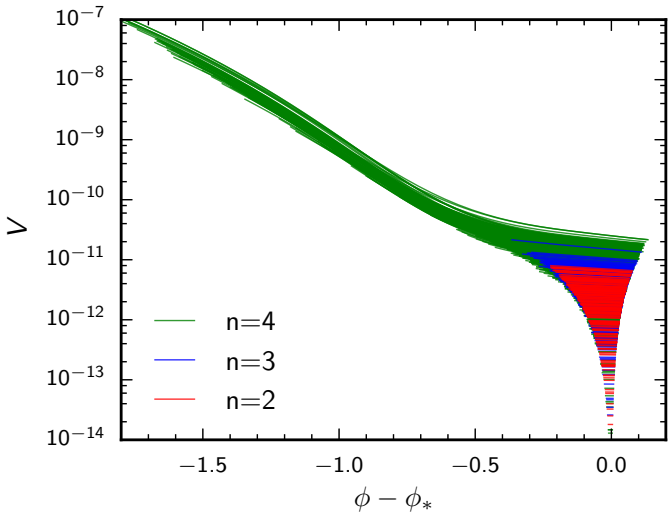

Fig. 20. Same as Fig. 15, when the Taylor expansion to nth order is performed on $H(\phi)$ instead of $V(\phi)$, and the potential is inferred from Eq. (60).

coefficients. The main two differences with respect to the results of Sect. 7.2 are as follows:

- The reconstructed potential shapes for $n = 4$ at the beginning of the observable window differ. Figure 20 shows that even steeper potentials are allowed than for the $V(\phi)$ method, with an even greater excursion of the inflaton field between Hubble crossing for the largest observable wavelengths and the pivot scale. This is because the $H(\phi)$ reconstruction does not rely on attractor solutions and automatically explores all valid potentials regardless of their initial field velocity.
- The best-fit models are different, since they do not explore the same parametric families of potentials. In particular, for $n = 4$, the best-fit models have a negligible tensor contribution, but the distributions still have thick tails towards large tensor-to-scalar ratios, so that the upper bound on $r_{0.002}$ is as high as in the previous $n = 4$ models, $r_{0.002} < 0.32$.

Note that $\varpi_{\rm H}^3$ can be significantly larger than unity for $n = 4$. This does not imply violation of slow roll within the observable range. By assumption, for all accepted models, $\epsilon_{\rm H}$ must remain smaller than unity over that range. In fact, for most of the green potentials visible in Fig. 20, we checked that $\epsilon_{\rm H}$ either has a maximum very close to unity near the beginning of the observable range or starts from unity. So the best-fit models (maximizing the power suppression at low multipoles) correspond either to inflation of short duration, or to models nearly violating slow roll just before the observable window. However, such peculiar models are not necessary for a good fit. Table 9 shows that the improvement in χ^2 as n increases is negligible.

In summary, this section further establishes the robustness of our potential reconstruction and two main conclusions. Firstly, under the assumption that the inflaton potential is smooth over the observable range, we showed that the simplest parametric forms (involving only three free parameters including the amplitude $V(\phi_*)$, no deviation from slow roll, and nearly power law primordial spectra) are sufficient to explain the data. No high-order derivatives or deviations from slow roll are required. Secondly, if one allows more freedom in the potential – typically, two more parameters – it is easy to decrease the large-scale primordial spectrum amplitude with an initial stage of "marginal slow roll" along a steep branch of the potential followed by a transition to a less steep branch. This type of model can accommodate a large tensor-to-scalar ratio, as high as $r_{0.002} \approx 0.3$.

8. $\mathcal{P}(k)$ reconstruction

In PCI13 (Sect. 7) we presented the results of a penalized likelihood reconstruction, seeking to detect any possible deviations from a homogeneous power-law form (i.e., $\mathcal{P}_{\mathcal{R}}(k) \propto k^{n_{\rm s}-1}$) for the primordial power spectrum (PPS) for various values of a smoothing parameter, λ. (For an extensive set of references to the prior literature concerning the methodology for reconstructing the power spectrum, see PCI13.) In the initial March 2013 preprint version of that paper, we reported evidence for a feature at moderate statistical significance around $k \approx 0.15\,{\rm Mpc}^{-1}$. However, in the November 2013 revision we retracted this finding, because subsequent tests indicated that the feature was no longer statistically significant when more aggressive cuts were made to exclude sky survey rings where contamination from electromagnetic interference from the 4 K cooler was largest, as indicated in the November 2013 "Note Added."

In this section we report on results using the 2015 $C_\ell^{\rm TT}$ likelihood (Sect. 8.1) using essentially the same methodology as described in PCI13. (See Gauthier & Bucher 2012, and references therein for more technical details.) This method is also extended to include the *EE* and *TE* likelihoods in Sect. 8.1.2. As part of this 2015 release, we include the results of two other methods (see Sects. 8.2 and 8.3) to search for features. We find that all three methods yield broadly consistent reconstructions and reach the following main conclusion: there is no statistically significant evidence for any features departing from a simple power-law (i.e., $\mathcal{P}_{\mathcal{R}}(k) \propto k^{n_{\rm s}-1}$) PPS. Given the substantial differences between these methods, it is satisfying to observe this convergence.

8.1. Method I: penalized likelihood

8.1.1. Update with 2015 temperature likelihood

We repeated the same maximum likelihood analysis used to reconstruct the PPS in PCI13 using the updated *Planck* TT+lowP likelihood. Since we are interested in deviations from the nearly scale-invariant model currently favoured by the parametric approach, we replaced the true PPS $\mathcal{P}_{\mathcal{R}}(k)$ by a fiducial power-law spectrum $\mathcal{P}_{\mathcal{R}}^{(0)}(k) = A_{\rm s}(k/k_*)^{n_{\rm s}-1}$, modulated by a small deviation function $f(k)$:

$$\mathcal{P}_{\mathcal{R}}(k) = \mathcal{P}_{\mathcal{R}}^{(0)}(k) \exp\left[f(k)\right]. \tag{65}$$

The deviation function $f(k)$[7] was represented by B-spline basis functions parameterized by $n_{\rm knot}$ control points $\boldsymbol{f} = \{f_i\}_{i=1}^{n_{\rm knot}}$, which are the values of $f(k)$ along a grid of knot points $\kappa_i = \ln k_i$.

Naively maximizing the *Planck* TT+lowP likelihood with respect to $\boldsymbol{f}$ results in over-fitting to cosmic variance and noise in the data. Furthermore, due to the limited range of scales over which *Planck* measures the anisotropy power spectrum, the likelihood is very weakly dependent on $f(k)$ at extremely small and large scales. To address these issues, the following two penalty functions were added to the *Planck* likelihood:

$$\begin{aligned}\boldsymbol{f}^{\rm T}\boldsymbol{R}(\lambda,\alpha)\boldsymbol{f} \equiv \lambda \int {\rm d}\kappa \left(\frac{\partial^2 f(\kappa)}{\partial \kappa^2}\right)^2 \\ + \alpha \int_{-\infty}^{\kappa_{\rm min}} {\rm d}\kappa\, f^2(\kappa) + \alpha \int_{\kappa_{\rm max}}^{+\infty} {\rm d}\kappa\, f^2(\kappa).\end{aligned} \tag{66}$$

[7] The definition of $f(k)$ used here differs from that of PCI13 in that $\exp(f)$ is used in place of $1 + f$ to ensure that the reconstructed primordial power spectrum is always non-negative.

The first term on the right-hand side of Eq. (66) is a roughness penalty, which disfavours $f(\kappa)$ that "wiggle" too much. The last two terms drive $f(\kappa)$ to zero for scales below $\kappa_{\rm min}$ and above $\kappa_{\rm max}$. The values of λ and α represent the strengths of the respective penalties. The exact value of α is unimportant as long as it is large enough to drive $f(\kappa)$ close to zero on scales outside $[\kappa_{\rm min}, \kappa_{\rm max}]$. However, the magnitude of the roughness penalty λ controls the smoothness of the reconstruction.

Since the anisotropy spectrum depends linearly on the PPS, the Newton-Raphson method is well suited to optimizing with respect to $\boldsymbol{f}$. However, a maximum likelihood analysis also has to take into account the cosmological parameters, $\boldsymbol{\Theta} \equiv \{H_0, \Omega_{\rm b}h^2, \Omega_{\rm c}h^2\}$[8]. These additional parameters are not easy to include in the Newton-Raphson method since it is difficult to evaluate the derivatives $\partial C_\ell/\partial\boldsymbol{\Theta}$, $\partial^2 C_\ell/\partial\boldsymbol{\Theta}^2$, etc., to the accuracy required by the method. Therefore a non-derivative method, such as the downhill simplex algorithm, is best suited to optimization over these parameters. Unfortunately the downhill simplex method is inefficient given the large number of control points in our parameter space. Since each method has its drawbacks, we combined the two methods to draw on their respective strengths. We define the function $\mathcal{M}$ as

$$\mathcal{M}(\boldsymbol{\Theta}) = \min_{f_i\in[-1,1]} \left\{-2\ln\mathcal{L}(\boldsymbol{\Theta}, \boldsymbol{f}) + \boldsymbol{f}^T\boldsymbol{R}(\lambda,\alpha)\boldsymbol{f}\right\}. \quad (67)$$

Given a set of non-PPS cosmological parameters $\boldsymbol{\Theta}$, $\mathcal{M}$ is the value of the penalized log likelihood, minimized with respect to $\boldsymbol{f}$ using the Newton-Raphson method. The function $\mathcal{M}$ is in turn minimized with respect to $\boldsymbol{\Theta}$ using the downhill simplex method. In contrast to the analysis done in PCI13, the *Planck* low-ℓ likelihood has been modified so that it can be included in the Newton-Raphson minimization. Thus the reconstructions presented here extend to larger scales than were considered in 2013.

Figure 21 shows the best-fit PPS reconstruction using the *Planck* TT+lowP likelihood. The penalties in Eq. (66) introduce a bias in the reconstruction by smoothing and otherwise deforming potential features in the power spectrum. To assess this bias, we define the "minimum reconstructible width" (MRW) to be the minimum width of a Gaussian feature needed so that the integrated squared difference between the feature and its reconstruction is less than 1% of the integrated square of the input Gaussian, which is equivalent to 10% rms. Due to the combination of the roughness and fixing penalties, it is impossible to satisfy the MRW criterion too close to $\kappa_{\rm min}$ and $\kappa_{\rm max}$. Wherever the MRW is undefined, the reconstruction is substantially biased and therefore suspect. An MRW cannot be defined too close to the endpoints $\kappa_{\rm min}$ and $\kappa_{\rm max}$ for two reasons: (1) lack of data; and (2) if a feature is too close to where the fixing penalty has been applied, the fixing penalty distorts the reconstruction. Consequently a larger roughness penalty decreases the range over which an MRW is well defined. The grey shaded areas in Fig. 21 show where the MRW is undefined and thus the reconstruction cannot be trusted. The cutoffs $\kappa_{\rm min}$ and $\kappa_{\rm max}$ have been chosen to maximize the range over which an MRW is defined for a given value of λ. The 1σ and 2σ error bars in Fig. 21 are estimated using the Hessian of the log-likelihood evaluated at the best-fit PPS reconstruction. More detailed MC investigations suggest that the nonlinear corrections to these error bars are small.

[8] Due to the high correlation between τ and $A_{\rm s}$, τ is not included as a free parameter. Any change in τ can be almost exactly compensated for by a change in $A_{\rm s}$. We fix τ to its best-fit fiducial model value.

For the $\lambda = 10^5$ and 10^6 cases of the TT reconstruction, no deviation exceeds 2σ, so we do not comment on the probability of obtaining a worse fit. For the other cases, we use the maximum of the deviation, expressed in σ, of the plotted points as a metric of the quality of fit. Then using Monte Carlo simulations, we compute the p-value, or the probability to obtain a worse fit, according to this metric. For $\lambda = 10^3$ and 10^4, we obtain p-values of 0.304 and 0.142, respectively, corresponding to 1.03 and 1.47σ. We thus conclude that the observed deviations are not statistically significant.

8.1.2. Penalized likelihood results with polarization

In Fig. 22 the best-fit reconstruction of the PPS from the *Planck* TT, TE, EE+lowP likelihood is shown. We observe that the reconstruction including polarization broadly agrees with the reconstruction obtained using temperature only. For the *Planck* TT, TE, EE+lowP likelihood, we obtain for $\lambda = 10^3$, 10^4, and 10^5 the p-values 0.166, 0.107, and 0.045, respectively, corresponding to 1.38, 1.61, and 2.00σ, and likewise conclude the absence of any statistically significant evidence for deviations from a simple power-law scalar primordial power spectrum.

8.2. Method II: Bayesian model comparison

In this section we model the PPS $\mathcal{P}_{\mathcal{R}}(k)$ using a nested family of models where $\mathcal{P}_{\mathcal{R}}(k)$ is piecewise linear in the $\ln(\mathcal{P})$-$\ln(k)$ plane between a number of knots, $N_{\rm knots}$, that is allowed to vary. The question arises as to how many knots one should use, and we address this question using Bayesian model comparison. A family of priors is chosen where both the horizontal and vertical positions of the knots are allowed to vary. We examine the "Bayes factor" or "Bayesian evidence" as a function of $N_{\rm knots}$ to decide how many knots are statistically justified. A similar analysis has been performed by Vázquez et al. (2012) and Aslanyan et al. (2014). In addition, we marginalize over all possible numbers of knots to obtain an averaged reconstruction weighted according to the Bayesian evidence.

The generic prescription is illustrated in Fig. 23. $N_{\rm knots}$ knots $\{(k_i, \mathcal{P}_i) : i = 1, \ldots, N_{\rm knots}\}$ are placed in the $(k, \mathcal{P}_{\mathcal{R}})$ plane and the function $\mathcal{P}_{\mathcal{R}}(k)$ is constructed by logarithmic interpolation (a linear interpolation in log-log space) between adjacent points. Outside the horizontal range $[k_1, k_N]$ the function is extrapolated using the outermost interval.

Within this framework, base ΛCDM arises when $N_{\rm knots} = 2$ – in other words, when there are two boundary knots and no internal knots, and the parameters $\mathcal{P}_1$ and $\mathcal{P}_2$ (in place of $A_{\rm s}$ and $n_{\rm s}$) parameterize the simple power-law PPS. There are also, of course, the four standard cosmological parameters ($\Omega_{\rm b}h^2$, $\Omega_{\rm c}h^2$, $100\theta_{\rm MC}$, and τ), as well as the numerous foreground parameters associated with the *Planck* high-ℓ likelihood, all of which are unrelated to the PPS. This simplest model can be extended iteratively by successively inserting an additional internal knot, thus requiring with each iteration two more variables to parameterize the new knot position.

We run models for a variety of numbers of internal knots, $N_{\rm int} = N_{\rm knots} - 2$, evaluating the evidence for $N_{\rm int}$. Under the assumption that the prior is justified, the most likely, or preferred, model is the one with the highest evidence. Evidences are evaluated using the `PolyChord` sampler (Handley et al. 2015) in `CAMB` and `CosmoMC`. The use of `PolyChord` is essential, as the posteriors in this parameterization are often multi-modal. Also, the ordered log-uniform priors on the k_i are easy to implement

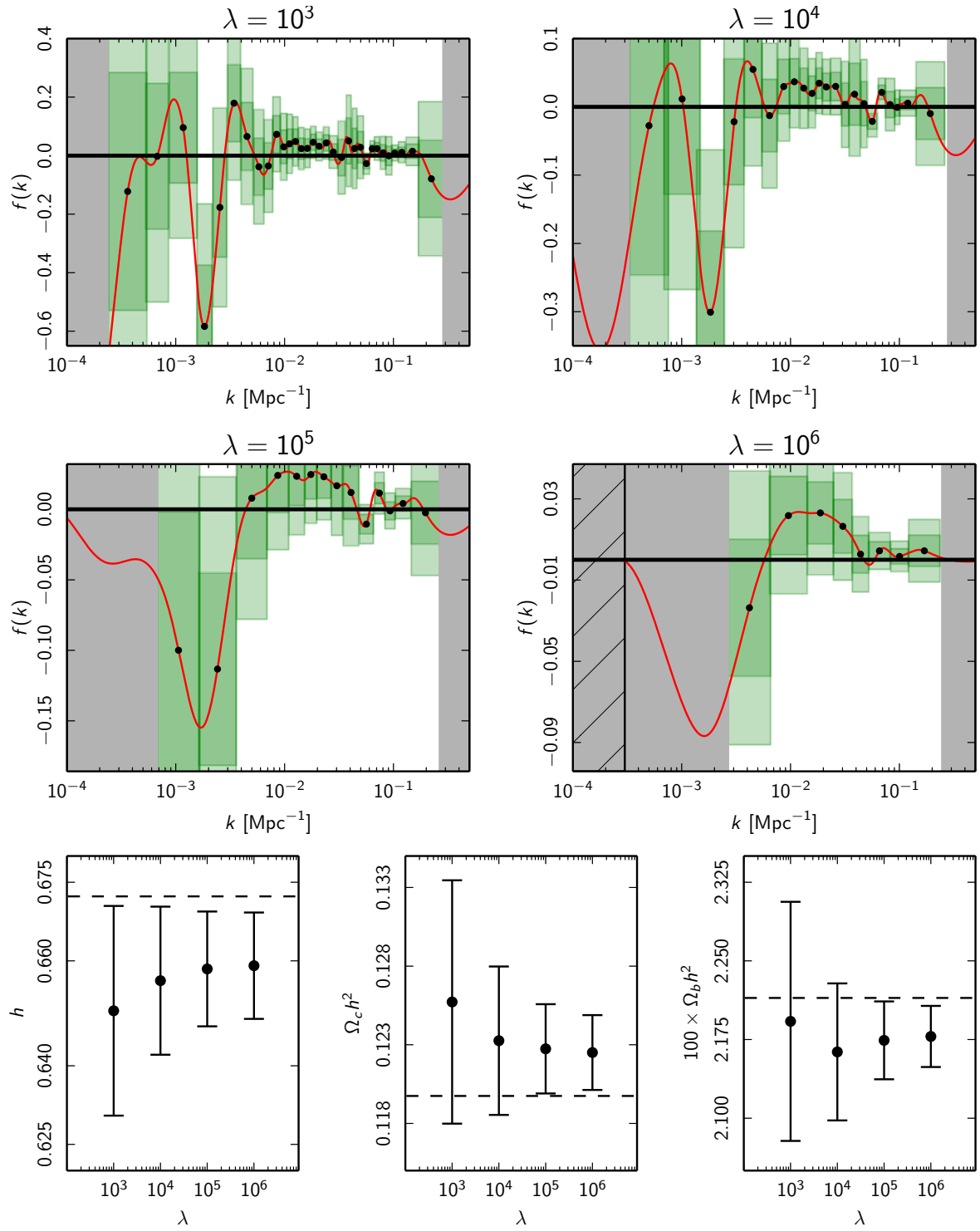

Fig. 21. *Planck* TT+lowP likelihood primordial power spectrum (PPS) reconstruction results. *Top four panels*: reconstruction of the deviation $f(k)$ using four different roughness penalties. The red curves represent the best-fit deviation $f(k)$ using the *Planck* TT+lowP likelihood. $f(k) = 0$ would represent a perfectly featureless spectrum with respect to the fiducial PPS model, which is obtained from the best-fit base ΛCDM model with a power-law PPS. The vertical extent of the dark and light green error bars indicates the $\pm 1\sigma$ and $\pm 2\sigma$ errors, respectively. The width of the error bars represents the minimum reconstructible width (the minimum width for a Gaussian feature so that the mean square deviation of the reconstruction is less than 10%). The grey regions indicate where the minimum reconstructible width is undefined, indicating that the reconstruction in these regions is untrustworthy. The hatched region in the $\lambda = 10^6$ plot shows where the fixing penalty has been applied. These hashed regions are not visible in the other three reconstructions, for which $\kappa_{\rm min}$ lies outside the range shown in the plots. For all values of the roughness penalty, all data points are within 2σ of the fiducial PPS except for the deviations around $k \approx 0.002\,{\rm Mpc}^{-1}$ in the $\lambda = 10^3$ and $\lambda = 10^4$ reconstructions. *Lower three panels*: $\pm 1\sigma$ error bars of the three non-PPS cosmological parameters included in the maximum likelihood reconstruction. All values are consistent with their respective best-fit fiducial model values indicated by the dashed lines.

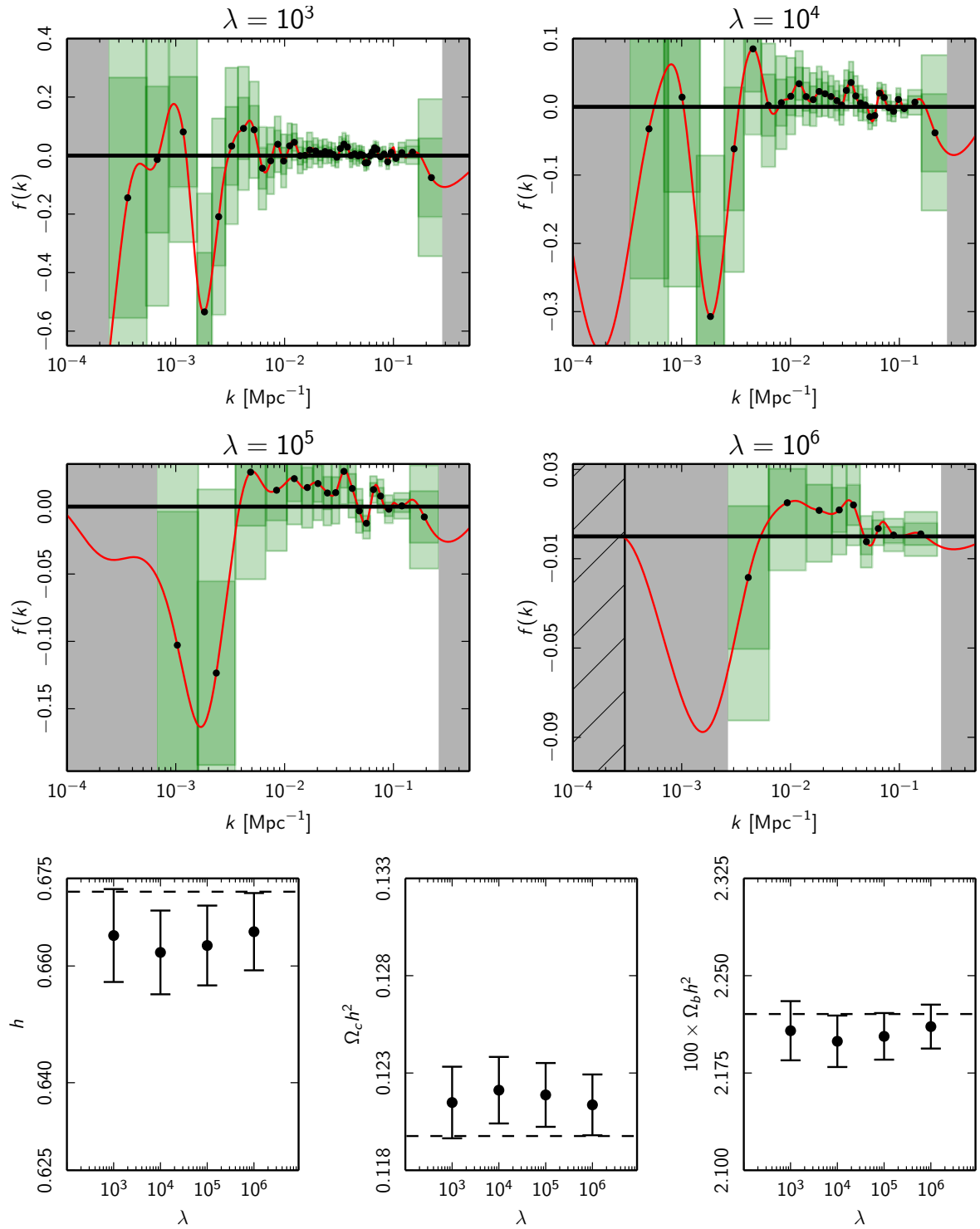

Fig. 22. *Planck* TT, TE, EE+lowP likelihood primordial power spectrum reconstruction results. *Top four panels*: reconstruction of the deviation $f(k)$ using four different roughness penalties. As in Fig. 21, the red curves represent the best-fit deviation $f(k)$ and the height and width of the green error bars represent the error and minimum reconstructible width, respectively. For all values of the roughness penalty, the deviations are consistent with a featureless spectrum. *Lower three panels*: $\pm 1\sigma$ error bars of the three non-PPS cosmological parameters included in the maximum likelihood reconstruction. All values are consistent with their respective best-fit fiducial model values (indicated by the dashed lines).

within the `PolyChord` framework. All runs were performed with 1000 live points, oversampling the semi-slow and fast parameters by a factor of 5 and 100, respectively.

Priors for the reconstruction parameters are detailed in Table 10. We report evidence ratios with respect to the base ΛCDM case. The cosmological priors remain the same for all models, and this part of the prior has almost no impact on the evidence ratios. The choice of prior on the reconstruction parameters $\{\mathcal{P}_i\}$ does affect the Bayes factor. `CosmoMC`, however, puts an implicit prior on all models by excluding parameter choices that render the internal computational approximations in `CAMB` invalid. The baseline prior for the vertical position of the

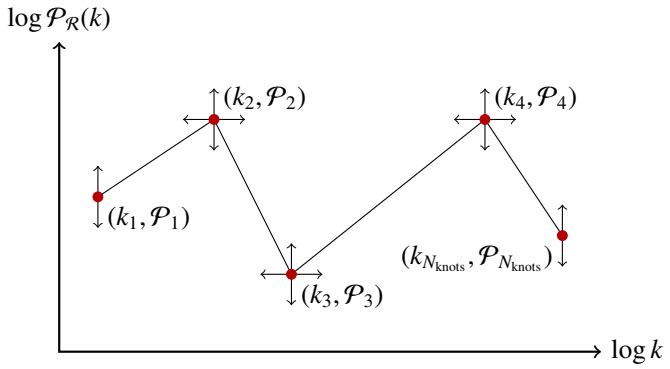

Fig. 23. Linear spline reconstruction. The primordial power spectrum is reconstructed using $N_{\rm knots}$ interpolation points $\{(k_i, \mathcal{P}_i)\colon i = 1, 2, \ldots, N_{\rm knots}\}$. The end knots are fixed in k but allowed to vary in $\mathcal{P}$, whereas the internal knots can vary subject to the constraint that $k_1 < k_2 < \cdots < k_{N_{\rm knots}}$. The function $\mathcal{P}_{\mathcal{R}}(k)$ is constructed within the range $[k_1, k_{N_{\rm knots}}]$ by interpolating logarithmically between adjacent knots (i.e., linearly in log-log space). Outside this range the function is extrapolated logarithmically. The function $\mathcal{P}_{\mathcal{R}}(k; \{k_i, \mathcal{P}_i\})$ thus has $2N_{\rm knots} - 2$ parameters.

Table 10. Prior for moveable knot positions.

Parameter range	Prior type
$10^{-4}\,\mathrm{Mpc}^{-1} = k_1 < k_2 < \ldots < k_{N_{\rm knots}} = 0.3\,\mathrm{Mpc}^{-1}$	log uniform (sorted)
$2 < \ln\left(10^{10}\mathcal{P}_1\right), \ldots, \ln\left(10^{10}\mathcal{P}_{N_{\rm knots}}\right) < 4$	log uniform
$2 \le N_{\rm knots} \le 10$	integer uniform

Notes. The $\mathcal{P}_{\mathcal{R}}$ positions are distributed in a log-uniform manner across a wide range. The k positions are also log-uniformly distributed across the entire range needed by `CosmoMC` and are sorted so that $k_1 < \ldots < k_{N_{\rm knots}}$. When we marginalize over the number of knots, $N_{\rm knots}$, we assume a uniform prior between 2 and 10.

knots includes all of the range allowed by `CosmoMC`, so slighly increasing this prior range will not affect the evidence ratios. If one were to reduce the prior widths significantly, the evidence ratios would be increased. The allowed horizontal range includes all k-scales accessible to *Planck*. Thus, altering this width would be unphysical.

After completion of an evidence calculation, `PolyChord` generates a representative set of samples of the posterior for each model, $P(\Theta) \equiv P(\Theta|\mathrm{data}, N_{\rm int})$. We may use this to calculate a marginalized probability distribution for the PPS:

$$P(\log \mathcal{P}_{\mathcal{R}}|k, N_{\rm int}) = \int \delta\left(\log \mathcal{P}_{\mathcal{R}} - \log \mathcal{P}_{\mathcal{R}}(k; \Theta)\right) P(\Theta)\, \mathrm{d}\Theta. \quad (68)$$

This expression encapsulates our knowledge of $\mathcal{P}_{\mathcal{R}}$ at each value of k for a given number of knots. Plots of this PPS posterior are shown in Fig. 24 using *Planck* TT data.

If one considers the Bayesian evidence of each model, Fig. 25 shows that although no model is preferred over base ΛCDM, the case $N_{\rm int} = 1$ is competitive. This model is analogous to the broken-power-law spectrum of Sect. 4.4, although the models differ significantly in terms of the priors used. In this case, the additional freedom of one knot allows a reconstruction of the suppression of power at low ℓ. Adding polarization data does not alter the evidences significantly, although $N_{\rm int} = 1$ is strengthened. We also plot a *Planck* TT run, but with the reduced vertical priors $2.5 < \ln\left(10^{10}\mathcal{P}_i\right) < 3.5$. As expected, this increases the evidence ratios, but does not alter the above conclusion.

For increasing numbers of internal knots, the Bayesian evidence monotonically decreases. Occam's razor dictates, therefore, that these models should not be preferred, due to their higher complexity. However, there is an intriguing stable oscillatory feature, at $20 \lesssim \ell \lesssim 50$, that appears once there are enough knots to reconstruct it. This is a qualitative feature predicted by several inflationary models (discussed in Sect. 9), and a possible hint of new physics, although its statistical significance is not compelling.

A full Bayesian analysis marginalizes over all models weighted according to the normalized evidence $Z_{N_{\rm int}}$, so that

$$P(\log \mathcal{P}_{\mathcal{R}}|k) = \sum_{N_{\rm int}} P(\log \mathcal{P}_{\mathcal{R}}|k, N_{\rm int}) Z_{N_{\rm int}}, \quad (69)$$

as indicated in Fig. 26. This reconstruction is sensitive to how model complexity is penalized in the prior distribution.

8.3. Method III: cubic spline reconstruction

In this section we investigate another reconstruction algorithm based on cubic splines in the $\ln(k)$-$\ln \mathcal{P}_{\mathcal{R}}$ plane, where (unlike for the approach of the previous subsection) the horizontal positions of the knots are uniformly spaced in $\ln(k)$ and fixed. A prior on the vertical positions (described in detail below) is chosen and the reconstructed power spectrum is calculated using `CosmoMC` for various numbers of knots. This method differs from the method in Sect. 8.1 in that the smoothness is controlled by the number of discrete knots rather than by a continuous parameter of a statistical model having a well-defined continuum limit. With respect to the Bayesian model comparison of Sect. 8.2, the assessment of model complexity differs because here the knots are not movable.

Let the horizontal positions of the n knots be given by k_b, where $b = 1, \ldots, n$, spaced so that k_{b+1}/k_b is independent of b. We single out a "pivot knot" $b = p$, so that $k_p = k_* = 0.05\,\mathrm{Mpc}^{-1}$, which is the standard scalar power spectrum pivot scale. For a given number of knots n we choose k_1 and k_n so that the interval of relevant cosmological scales, taken to extend from $10^{-4}\,\mathrm{Mpc}^{-1}$ to $O(1)\,\mathrm{Mpc}^{-1}$, is included. We now define the prior on the vertical knot coordinates. For the pivot point, we define $\ln A_{\rm s} = \ln \mathcal{P}_{\mathcal{R}}(k_*)$, where $\ln A_{\rm s}$ has a uniformly distributed prior, and for the other points with $b \neq p$, we define the derived variable

$$q_b \equiv \ln\left(\frac{\mathcal{P}_{\mathcal{R}}(k_b)}{\mathcal{P}_{\mathcal{R},\rm fid}(k_b)}\right), \quad (70)$$

where $\mathcal{P}_{\mathcal{R},\rm fid}(k) \equiv A_{\rm s}(k/k_*)^{n_{\rm s,fid}-1}$. Here the spectral index $n_{\rm s,fid}$ is fixed. A uniform prior is imposed on each variable q_b $(b \neq p)$ and the constraint $-1 \le q_b \le 1$ is also imposed to force the reconstruction to behave reasonably near the endpoints, where it is hardly constrained by the data. The quantity $\ln \mathcal{P}_{\mathcal{R}}(k)$ is interpolated between the knots using cubic splines with natural boundary conditions (i.e., the second derivatives vanish at the first and the last knots). Outside $[k_1, k_n]$ we set $\mathcal{P}_{\mathcal{R}}(k) = \mathrm{e}^{q_1}\mathcal{P}_{\mathcal{R},\rm fid}(k)$ (for $k < k_1$) and $\mathcal{P}_{\mathcal{R}}(k) = \mathrm{e}^{q_n}\mathcal{P}_{\mathcal{R},\rm fid}(k)$ (for $k > k_n$). For most knots, we found that the upper and lower bounds of the q_b prior hardly affect the reconstruction, since the data sharpen the allowed range significantly. However, for super-Hubble scales (i.e., $k \lesssim 10^{-4}\,\mathrm{Mpc}^{-1}$) and very small scales (i.e., $k \gtrsim 0.2\,\mathrm{Mpc}^{-1}$), which are only weakly constrained by the cosmological data, the prior dominates the reconstruction. For the results here, a fiducial

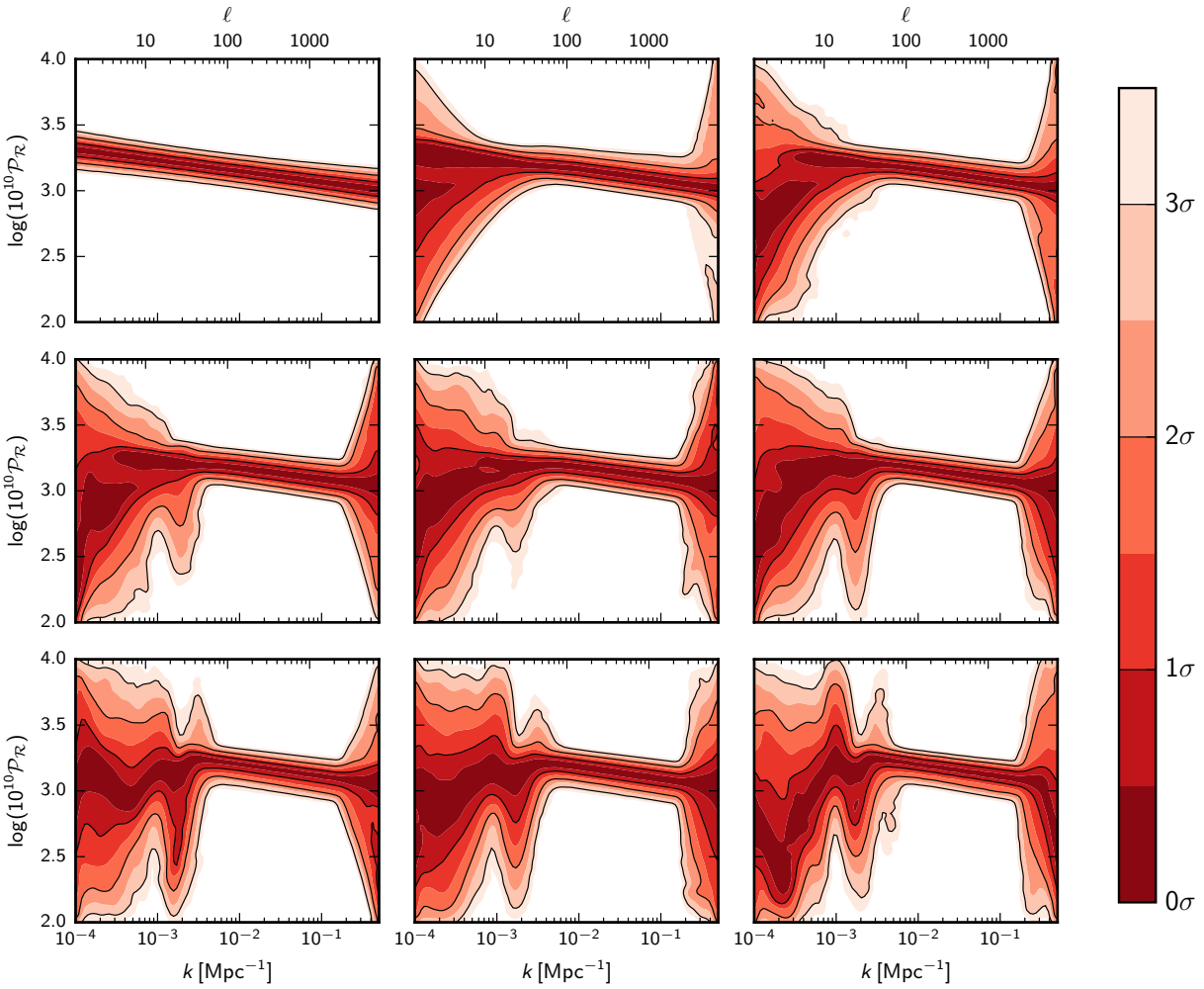

Fig. 24. Bayesian movable knot reconstructions of the primordial power spectrum $\mathcal{P}_{\mathcal{R}}(k)$ using *Planck* TT data. The plots indicate our knowledge of the PPS $P(\mathcal{P}_{\mathcal{R}}(k)|k, N_{\rm int})$ for a given number of knots. The number of internal knots $N_{\rm int}$ increases (*left to right and top to bottom*) from 0 to 8. For each k-slice, equal colours have equal probabilities. The colour scale is chosen so that darker regions correspond to lower-σ confidence intervals. 1σ and 2σ confidence intervals are also indicated (black curves). The upper horizontal axes give the approximate corresponding multipoles via $\ell \approx kD_{\rm rec}$, where $D_{\rm rec}$ is the comoving distance to recombination.

spectral index $n_{\rm s,fid} = 0.967$ for $\mathcal{P}_{\mathcal{R},\rm fid}$ was chosen, which is close to the estimate from *Planck* TT+lowP+BAO. A different choice of $n_{\rm s,fid}$ leads to a trivial linear shift in the q_b.

The possible presence of tensor modes (see Sect. 5) has the potential to bias and introduce additional uncertainty in the reconstruction of the primordial scalar power spectrum as parameterized above. Obviously, in the absence of a detection of tensors at high statistical significance, it is not sensible to model a possible tensor contribution with more than a few degrees of freedom. A complicated model would lead to prior dominated results. We therefore use the power law parameterization, $\mathcal{P}_{\rm t}(k) = rA_{\rm s}(k/k_*)^{n_{\rm t}}$, where the consistency relation $n_{\rm t} = -r/8$ is enforced as a constraint.

Primordial tensor fluctuations contribute to CMB temperature and polarization angular power spectra, in particular at spatial scales larger than the recombination Hubble length, $k \lesssim (aH)_{\rm rec} \approx 0.005\,{\rm Mpc}^{-1}$. If a large number of knots in $\ln\mathcal{P}_{\mathcal{R}}(k)$ is included over that range, then a modified $\mathcal{P}_{\mathcal{R}}$ can mimic a tensor contribution, leading to a near-degeneracy. This can lead to large uncertainty in the tensor amplitude, r. Once r is measured or tightly constrained in B-mode experiments, this near degeneracy will be broken. As examples here, we do allow r to float, but also show what happens when r is constrained to take the values $r = 0.1$ and $r = 0.01$ in the reconstruction.

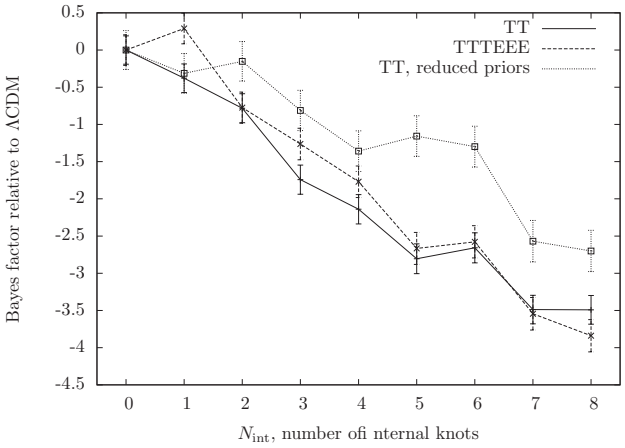

Fig. 25. Bayes factor (relative to the base ΛCDM model) as a function of the number of knots for three separate runs. Solid line: *Planck* TT. Dashed line: *Planck* TT, TE, EE. Dotted line: *Planck* TT, with priors on the $\mathcal{P}_i$ parameters reduced in width by a factor of 2 ($2.5 < \ln(10^{10}\mathcal{P}_i) < 3.5$).

Figure 27 shows the reconstruction obtained using the 2015 *Planck* TT+lowP likelihood, BAO, SNIa, HST, and a $z_{\rm re} > 6$